Synthesis and Characterization of Ce-doped TiO_2 Nanoparticles for Pharmaceutical Antibiotic Degradation

Dissertation submitted to

Visvesvaraya National Institute of Technology, Nagpur

in partial fulfillment of the requirements for the award of

the degree

Master of Science

in

Physics

by

Anisha Sahu

(MS23PHY001)

Under the guidance of

Prof. R. S. Gedam

Department of Physics

Visvesvaraya National Institute of Technology

Nagpur 440 010 (India)

2023-25

Synthesis and Characterization of Ce-doped TiO_2 Nanoparticles for Pharmaceutical Antibiotic Degradation

Dissertation submitted to

Visvesvaraya National Institute of Technology, Nagpur

in partial fulfillment of the requirements for the award of

the degree

Master of Science

in

Physics

by

Anisha Sahu

(MS23PHY001)

Under the guidance of

Prof. R. S. Gedam

Department of Physics

Visvesvaraya National Institute of Technology

Nagpur 440 010 (India)

2023-25

Department of Physics

Visvesvaraya National Institute of Technology, Nagpur

© Visvesvaraya National Institute of Technology (VNIT) 2009

Department of Physics

Visvesvaraya National Institute of Technology, Nagpur

Dissertation Approval Sheet

Dissertation entitled — **"Synthesis and Characterization of Ce-doped TiO_2 Nanoparticles for Pharmaceutical Antibiotic Degradation"** by Anisha Sahu is approved for the degree of Master of Science in Physics.

_____ _____

(Name:) (Name:)

Supervisor **External Exainer**

_____

(Name:)

Chairman
Date
Place:

Department of Physics

Visvesvaraya National Institute of Technology, Nagpur

Declaration

I, Anisha Sahu, hereby declare that this dissertation titled **"Synthesis and Characterization of Ce doped TiO_2 Nanoparticles for Pharmaceutical Antibiotic Degradation"** is carried out by me in the Department of Physics of Visvesvaraya National Institute of Technology, Nagpur. The work is original and has not been submitted earlier whole or in part for the award of any degree/diploma at this or any other Institution / University.

Anisha Sahu

Date:

Certificate

This is to certify that the dissertation titled **"Synthesis and Characterization of Ce-doped TiO_2 Nanoparticles for Pharmaceutical Antibiotic Degradation"** is submitted by **Anisha Sahu** in partial fulfillment of the requirements for the award of the degree of **Master of Science in Physics**, VNIT Nagpur. The work is comprehensive, complete, and fit for final evaluation.

Supervisor,

Dr. R. S. Gedam

Professor

Dept. of Physics, VNIT, Nagpur

Head, Department of Physics

VNIT, Nagpur

Date:

Department of Physics

Visvesvaraya National Institute of Technology, Nagpur

Non- Plagiarism Certificate

Certified that M.Sc. Dissertation titled **"Synthesis and Characterization of Ce-doped TiO_2 Nanoparticles for Pharmaceutical Antibiotic Degradation**" submitted by **Anisha Sahu**, Enrollment no. **MS23PHY001**, ID No. **30067** has been checked for plagiarism using TURNITIN software, and overlap is found within prescribed limits (<30%). A summary of the report is given below:

ORIGINALITY REPORT			
20%	14%	16%	8%
SIMILARITY INDEX	INTERNET SOURCES	PUBLICATIONS	STUDENT PAPERS

Anisha Sahu
(MS23PHY001)
ID No: 30067

Dr. R.S Gedam
Professor
Department of Physics
VNIT, Nagpur

ACKNOWLEDGMENT

At the outset of this thesis, I would like to express my heartfelt and sincere gratitude to all those who supported, guided, and encouraged me throughout my research journey. Their invaluable contributions have been instrumental in the successful completion of this project.

I am sincerely obliged to **Prof. R. S. Gedam** from the Department of Physics at VNIT Nagpur, Maharashtra, for his continuous support, excitement and valuable guidance during the course of my research journey. His insightful suggestions, continuous encouragement, and enduring mentorship have played a pivotal role in shaping the progress and success of my work. His dedication to scientific inquiry, meticulous approach, elderly support and inspiring attitude have significantly contributed to my academic development. I truly appreciate his allegiance and the fundamental role he has played in helping me accomplish this landmark.

I would also like to convey my deep recognition to **Miss. Ashwini S. Gadge** for her unfaltering support, encouragement, dedicated assistance and continuous presence throughout my work.

I genuinely thank **Miss. Yogita Shendre** and **Mr. Abhay Masram** for their encouragement and crucial advice.

A deep gratitude and sincere appreciation go to my parents and family members for their unwavering affection, moral support, encouragement and financial backing.

I am also gratified to my lab-mate, Miss Abhilasha Kumari, for her warmth, partnership, and ongoing assistance, both throughout the lab work and in all other aspects.

Ultimately, I would like to appreciate my friends and classmates for their unwavering encouragement, collaboration, and understanding. Their companionship has played a crucial role throughout my journey.

(Anisha Sahu)

ABSTRACT

In the present study, Ce-doped TiO_2 nanoparticles were successfully synthesized by using a hydrothermal method via green synthesis route using *Piper betel* leaves extract. Various characterization was implemented to analyze the prepared nanoparticles, including TGA-DTA, XRD, Raman, FTIR, SEM with EDS, UV-Visible, and PL analysis. XRD and Raman spectra confirmed the crystalline anatase phase of TiO_2 present in the prepared samples. FTIR spectra revealed structural changes occurred due to the incorporation of Ce into TiO_2 lattice structure. The surface morphology and elemental composition was analyzed by SEM-EDS analysis. UV-Vis absorption studies revealed the red shift in the absorption edge towards the visible region, indicating enhanced light absorption with Ce doping. Furthermore, more efficient charge carrier separation and a reduction in recombination rates was confirmed by PL analysis. The prepared samples were tested for ciprofloxacin antibiotic degradation under visible irradiation and sample with the lowest PL intensity CeT_0.9 shows the highest degradation efficiency (98.25%) in 120 minutes. The obtained results emphasize the significant prospects of Ce-doped TiO_2 as an optimal photocatalyst for environmental remediation.

LIST OF FIGURES

FIGURE NO.	PARTICULARS	PAGE NO.
1.1	Chemical structure of ciprofloxacin (CIP)	3
1.2	Mechanism of photocatalysis	5
3.1	Synthesis of Ce doped TiO2 nanoparticles by hydrothermal method using green synthesis	20
3.2	HITACHI STA7200	22
3.3	Schematic diagram of X-ray diffractometer	23
3.4	D8 quest system (Bruker diffractometer)	24
3.5	Schematic representation of energy states participating in Raman spectroscopy	25
3.6	Experimental setup of NOST: HEDA-URSM4/5/7 Raman spectrometer	26
3.7	JASCO FTIR-4600 spectrometer	27
3.8	Experimental setup of SEM	28
3.9	Schematic representation of ZEISS evo SEM18, SEM instrument	29
3.10	Ray-diagram of double beam spectrophotometer	30
3.11	JASCO V-670, UV-Vis-NIR spectrophotometer	31
3.12	Energy level diagram for electronic transition	32

3.13	**JASCO FP 8200 Spectroflurometer**	**33**
4.1	**TGA-DTA curves of synthesized samples.**	**35**
4.2	**XRD of prepared samples.**	**37**
4.3	**Raman spectra of synthesized samples**	**38**
4.4	**FTIR of prepared samples**	**39**
4.5	**Surface morphology of (a) CeT_0, (b) CeT_0.3, (c) CeT_0.5, (d) CeT_0.7, (e) CeT_0.9, and (f) EDS and (g) elemental mapping of CeT_0.9**	**40**
4.6	**UV-Vis spectra of prepared samples**	**41**
4.7	**Tauc's plot of prepared samples**	**42**
4.8	**PL spectra of prepared samples**	**43**
5.1	**UV-Vis absorption spectra of CIP degradation with CeT_0.9**	**46**
5.2	**Relative concentration of CIP with irradiation time**	**47**
5.3	**Plot of ln(C0/Ct) against irradiation time**	**48**
5.4	**Reusability study for CeT-0.9 Photocatalyst**	**49**
5.5	**Mechanism of degradation of CIP using prepared sample**	**51**

LIST OF TABLES

TABLE NO.	PARTICULARS	PAGE NO.
1.1	Basic information about ciprofloxacin (CIP)	3
3.1	Identifications of prepared photocatalysts	21
4.1	Calculated average crystallite size of all synthesized nanoparticles	36
4.2	Calculated energy band gap for prepared samples	42
5.1	Determined degradation efficiency and reaction rate of all photocatalyst	48

INDEX

S. No.	Chapter / Section Title	Page No.
—	Abstract	i
—	List of Figures	ii
—	List of Tables	iv
—	Index	v
1	**CHAPTER 1: INTRODUCTION**	
1.1	Pollution from Pharmaceutical Wastewater: An Increasing Environmental Risk	2
1.2	Effect of Antibiotics and Dyes on the Environment	2
1.2.1	Emerging Environmental Contaminants: Antibiotics	3
1.3	Dye Nominated for Photocatalytic Activity	3
1.4	Progressive Methods for Antibiotic Elimination from Waste Water	4
1.5	Photocatalysis	5
1.5.1	Mechanism of Photocatalysis	5
1.5.2	Semiconductors for Photocatalysis	6
1.6	Nanoparticles	7
1.7	TiO_2 Nanoparticles	8
1.8	Doping in TiO_2 Nanoparticles	9
1.9	Synthesis of TiO_2 Nanoparticles	10
1.10	Eco conscious Synthesis of TiO_2 Nanoparticles Using *Piper betel* Leaves	10
1.11	Hydrothermal Method	11
2	**CHAPTER 2: LITERATURE REVIEW AND METHODOLOGY**	
2.1	Literature Review	13
2.2	Objective	16
2.3	Methodology	17
3	**CHAPTER 3: SYNTHESIS OF MATERIAL AND CHARACTERIZATION TECHNIQUES**	
3.1	Synthesis of Materials	19
3.1.1	Materials and Reagents	19
3.1.2	Synthesis of Cerium Doped TiO_2 Nanoparticles	19
3.2	Characterization Techniques	21
3.2.1	TGA-DTA Study	22
3.2.2	X-Ray Diffraction Spectroscopy	23
3.2.3	Raman Spectroscopy	25
3.2.4	Fourier Transform Infrared (FTIR) Spectroscopy	26

S. No.	Chapter / Section Title	Page No.
3.2.5	Scanning Electron Microscopy (SEM)	28
3.2.5.1	Energy-Dispersive X-ray Spectroscopy (EDS or EDX)	29
3.2.6	UV-Visible Spectroscopy	30
3.2.7	Photoluminescence Spectroscopy	32
4	**CHAPTER 4: RESULTS AND DISCUSSION**	
4.1	TGA-DTA Study	35
4.2	XRD Analysis	36
4.3	Raman Analysis	37
4.4	FTIR	38
4.5	SEM	39
4.6	UV-Vis Analysis	40
4.7	Photoluminescence Study	43
5	**CHAPTER 5: DEGRADATION OF CIPROFLOXACIN ANTIBIOTIC**	
5.1	Experiment	45
5.2	Result	45
5.3	Reusability	49
5.4	Mechanism	50
6	**CHAPTER 6: CONCLUSION AND FUTURE SCOPE**	
6.1	Conclusion	53
6.2	Future Scope	53
	REFERENCES	54

CHAPTER 1
INTRODUCTION

CHAPTER 1
INTRODUCTION

1.1 Pollution from Pharmaceutical Wastewater: An Increasing Environmental Risk

The demand for pharmaceuticals has spiked due to accelerated industrial expansion, which has markedly improved human health and lifespan. However, this advancement has brought out the generation of considerable amount of wastewater impregnated with pharmaceutical substances. As a result, unrefined or inadequately managed wastewater is often released into water bodies, presenting significands threats to environmental habitats and human health. Pharmaceutical wastewater generally comprises resilient organic pollutants, synthetic dyes, and antibiotics that withstand conventional treatment procedures and tend to converge in water sources which used for drinking and cultivation. This pollution assists to the appearance of drug-refractory bacteria, shakes up endocrine regulation in aquatic creatures, and causes prolonged contamination of untainted water sources [1]. Despite the presence of legislative measures, the weak enforcement and inadequate supervision in a multitude of areas magnify the environmental hazards linked to pharmaceutical waste, underscoring the pressing need for more rigorous guidelines and upgraded treatment strategies [2].

Many pharmaceutical antibiotics are hydrophilic in nature, as they willingly incorporate into water, enabling them to promptly mix and diffuse in aquatic ecosystems. This contaminated water may promote the growth of bacteria in drains and pipelines. The high pH and temperature of this effluent will damage the environment. During wastewater evaporation, chemicals are united with air and cause allergic symptoms [3]. The development of sophisticated and environmentally friendly treatment systems is required due to the growing concern over pharmaceutical wastewater pollution.

1.2 Effect of Antibiotics and Dyes on the Environment

Because dyes are permanent and non-biodegradable, they have become a major environmental concern despite being widely used in the food, textile, and pharmaceutical industries. 15-50% of industrial dyes are discharged into water bodies without proper treatment, which pollutes the water and prevents aquatic photosynthesis [4]. These dyes'

stable aromatic structure not only makes them difficult to break down, but it also produces harmful byproducts that can cause cancer and mutagenesis in living things.

1.2.1 Emerging Environmental Contaminants: Antibiotics

Despite being essential for both human and animal health, antibiotics have become a serious environmental hazard. Only 30% of antibiotics that are provided are metabolized, according to research; the remaining 70% find their way into water systems through pharmaceutical companies, hospital effluents, and agricultural runoff [5]. These residues endanger aquatic life, change microbial populations, and encourage bacteria resistant to antibiotics.

1.3 Dye Nominated for Photocatalytic Activity

Ciprofloxacin is one of the most common antibiotics used widely. Ciprofloxacin (CIP) ($C_{17}H_{18}FN_3O_3$) is a second-generation antibiotic belonging to the fluoroquinolone class. It is commonly prescribed for the treatment of various infections, including typhoid fever, urinary tract infections, skin, bone, and joint infections, as well as gastrointestinal disorders [6]. Ciprofloxacin is highly stable and difficult to degrade by conventional water treatment methods. It is found in many water bodies, posing a serious threat to the environment.

Basic information on ciprofloxacin is given in the table:

Table 1.1 – Basic information about ciprofloxacin (CIP) [7]

MOLECULAR FORMULA	MOLECULAR WEIGHT
$C_{17}H_{18}FN_3O_3$	331.34 g/mol

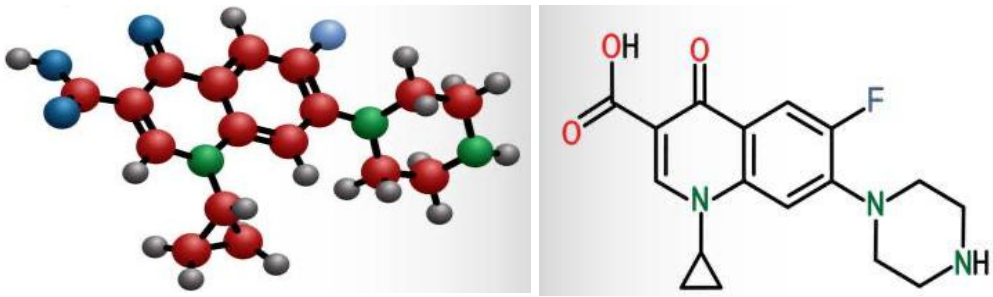

Fig.1.1 Chemical structure of ciprofloxacin (CIP)

Ciprofloxacin has a hydrophilic nature, so it easily mixes with water bodies. Due to its highly stable chemical structure, the by-products of ciprofloxacin are hard to degrade. Therefore, we need an efficient photocatalytic method to degrade CIP, as it cannot be degraded by conventional water treatment methods.

1.4 Progressive Methods for Antibiotic Elimination from Waste Water

The release of antibiotic into water systems presents a severe ecological hazard, driving the development of diverse elimination strategies. Traditional approaches—including biological degradation, adsorption processes, chemical oxidation, membrane filtration, and physio-chemical treatments—have been extensively utilized for dye removal [8]. Nevertheless, these techniques frequently suffer from drawbacks such as excessive operational expenses, time-intensive procedures, and suboptimal effectiveness, especially in industrial applications. Furthermore, certain conventional methods generate dangerous secondary contaminants, compounding environmental concerns. To address these limitations, AOPs (Advanced Oxidation Processes) have gained prominence as an innovative solution for antibiotic decomposition [9]. Techniques like ozonation, cavitation and photocatalytic oxidation fall under AOPs and are considered environmentally friendly, as they generate highly reactive species such as hydroxyl radicals, capable of rapidly and effectively degrading complex pollutants into simpler, less toxic compounds [10].

The underlying reaction mechanism can be expressed as:

Organic contaminant + $OH^{\bullet}$ → CO_2 + H_2O + mineral salts eq. (1.1)

AOPs offer significant benefits compared to traditional methods, such as:

- ➢ Rapid pollutant breakdown
- ➢ Negligible toxic residue formation
- ➢ Complete mineralization of organic compounds
- ➢ Environmentally sustainable and cost-efficient operation
- ➢ Compatibility with ambient temperature and pressure conditions

Moreover, photocatalysts employed in AOPs are often reusable and self-regenerating, improving process economics. These advantages establish AOPs as a state-of-the-art technology for sustainable wastewater remediation.

1.5 Photocatalysis

Photocatalytic reaction is a chemical process driven by the combined effect of light and a photocatalyst, enabling the complete degradation of pollutants into harmless substances.

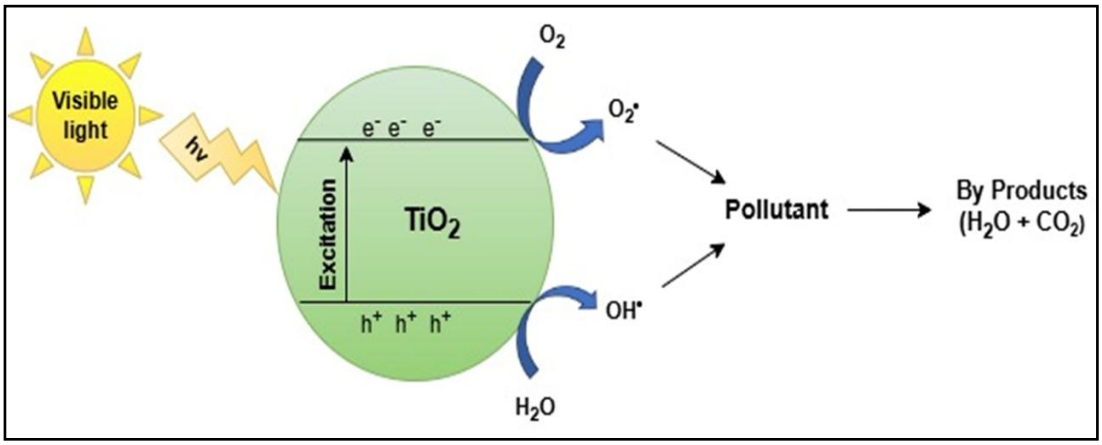

Fig. 1.2 Mechanism of photocatalysis

This technique is environmentally friendly, efficient, and helps prevent secondary pollution, making it a sustainable solution for environmental cleanup [11]. This approach is thought to be economical, environmentally friendly, and sustainable. A semiconductor catalyst absorbs light, which causes electrons in the valence band to be excited and move into the conduction band, forming electron-hole pairs. These charge carriers produce extremely reactive oxidizing species like superoxide anions (O_2^{-}•) and hydroxyl radicals (OH•) when they mix with oxygen and water molecules. Complex organic contaminants are broken down into less dangerous, simpler molecules by these radicals [12]. Because of the entire procedure, photocatalysis is a very effective and adaptable wastewater treatment method.

1.5.1 Mechanism of Photocatalysis

The photocatalytic mechanism is initiated by the absorption of light energy by the semiconductor photocatalyst. When the energy of the incident photons is equal to or exceeds the bandgap of the material, electrons in the valence band (VB) gain enough energy to transition to the conduction band (CB), resulting in the formation of electron-hole pairs. This process can be described by the following equation

$$\textbf{Photocatalyst} + h\nu \rightarrow e^{-}\ \textbf{(CB)} + h^{+}\ \textbf{(VB)} \qquad \text{eq. (1.2)}$$

The photoexcited charge carriers participate in surface redox reactions. The holes in the VB (valence band) oxidize water molecules or hydroxyl ions present on the catalyst surface, forming (OH•) hydroxyl radicals, which are highly reactive oxidizing species:

$$h^+ + H_2O \rightarrow OH\bullet + H^+ \quad \text{eq. (1.3)}$$

$$h^+ + OH^- \rightarrow OH \quad \text{eq. (1.4)}$$

Simultaneously, the charge carriers in the conduction band (e^-) interact with dissolved oxygen molecules, resulting in the formation of superoxide anions ($O_2^-\bullet$):

$$e^- + O_2 \rightarrow O_2^-\bullet \quad \text{eq. (1.5)}$$

$$O_2^-\bullet + H^+ \rightarrow HO_2\bullet \quad \text{eq. (1.6)}$$

$$2HO_2\bullet \rightarrow H_2O_2 + O_2 \quad \text{eq. (1.7)}$$

Hydrogen peroxide (H_2O_2) further decomposes into hydroxyl radicals, contributing to the degradation process:

$$H_2O_2 \rightarrow 2OH\bullet \quad \text{eq. (1.8)}$$

The generated hydroxyl radicals (OH•) and superoxide anions ($O_2^-\bullet$) act as primary reactive species responsible for breaking down organic contaminants into harmless by-products like carbon dioxide (CO_2) and water (H_2O). This entire chain of redox reactions makes photocatalysis an efficient and eco-friendly method for wastewater treatment applications.

1.5.2 Semiconductors for Photocatalysis

Semiconductor materials play a crucial role in photocatalysis owing to their ability to absorb light and produce electron-hole pairs. The effectiveness of a semiconductor as a photocatalyst depends on various factors:

- Optimal band gap energy to absorb visible or ultraviolet light,
- High charge carrier mobility to enhance electron transport,

- Non-toxic and eco-friendly nature,
- Chemical and thermal stability under reaction conditions,
- Large surface area for better adsorption of pollutants,
- Strong light absorption capacity,
- Low cost and natural abundance.

Several semiconductor nanomaterials have been explored for photocatalytic applications, including metal oxides (ZnO, WO_3, TiO_2), metal sulfides (ZnS, CdS, WS_2), and metal selenides (ZnSe, CdSe). Among these, titanium dioxide (TiO_2) stands out as the most widely used photocatalyst due to its affordability, chemical inertness, non-toxicity, excellent photocatalytic efficiency, superior photostability and healthy reduction properties [13].

1.6 Nanoparticles

Nanoparticles are materials with dimensions generally falling within the 1 to 100 nanometers scale, placing them in a unique regime between individual atoms and bulk matter. At this scale, materials demonstrate distinct physical, chemical, electrical, and optical characteristics that differ markedly from their larger counterparts. These unique behaviors primarily arise from the Quantum Confinement Effect, which take place when the particle size becomes comparable to the electron's de Broglie wavelength. This confinement modifies the electronic structure, leading to discrete energy levels rather than continuous energy bands. The extent of this effect depends on both the particle size and the Bohr radius of the material. One of the most notable features of nanoparticles is their high surface-area-to-volume ratio, which considerably boosts their surface interaction capabilities [14]. This property makes them especially attractive for applications in catalysis. Furthermore, the ability to tune the bandgap and control other optical characteristics through size and morphology adjustments makes nanoparticles highly valuable across diverse fields, including photocatalysis, biomedical engineering, optoelectronics, and sensor technologies.

Among several semiconductor nanomaterials, TiO_2 is extensively explored for its chemical inertness, non-toxicity and biocompatibility [15].

1.7 TiO_2 Nanoparticles

Titanium dioxide, often referred to as TiO_2 or titania, has been the subject of extensive research globally, resulting in a wealth of publications that investigate its various applications. In this project, TiO_2 is utilized as a photocatalyst. This compound is naturally present in several minerals, with ilmenite ore being the primary source for its commercial extraction. In its unrefined state, TiO_2 appears as a yellowish opaque material, which is subsequently processed into a white powder. TiO_2 can manifest in three distinct crystal structures: anatase, rutile, and brookite, with anatase and rutile both exhibiting tetragonal arrangement, whereas brookite forms an orthorhombic structure. Among these forms, the anatase phase is particularly noted for its outstanding photocatalytic performance, which can be ascribed to its lower density, improved electron mobility, and lower dielectric constant [16]. The unique characteristics of TiO_2 nanoparticles have garnered considerable interest, including:

- Non-toxic properties
- Broad absorption spectrum
- Strong oxidizing capabilities
- Chemical inertness
- High stability
- Cost-effectiveness
- Insolubility in water
- Natural abundance

These qualities render TiO_2 highly versatile, facilitating its application in various fields such as antimicrobial treatments, air purification, dye degradation, self-cleaning surfaces,

and hydrogen production. Nevertheless, TiO_2 faces certain challenges, including a broad bandgap with anatase exhibiting a value of 3.2 eV and a high rate of electron-hole pair recombination, which limit its photocatalytic efficiency when exposed to visible light [17].

1.8 Doping in TiO_2 Nanoparticles

Doping is an impactful technique to tailor the structural, optical, and electronic behavior of semiconducting materials and it also plays a crucial role in shifting the band position and tuning the bandgap of TiO_2, while simultaneously enhancing the carrier concentration and extending the lifespan of charge carriers [18]. Doping improves the optical response by shifting the absorption region toward longer wavelengths in the visible range, resulting in a significant narrowing of the bandgap energy [19]. This effect makes TiO_2 photo catalytically active under visible light irradiation. Doping also plays a pivotal role in suppressing the recombination process and hence promotes photocatalytic performance.

Rare earth metals, particularly lanthanide elements, have drawn significant focus due to their unique electronic configuration and catalytic properties. Rare earth ions possess incompletely filled 4f orbitals, which can serve as electron capture site and reduce the electron-hole recombination rate. Additionally, rare earth ions are capable of forming complexes with Lewis bases, thereby improving the adsorption capacity of TiO_2 on the dye surface during the photocatalytic process [20].

Cerium (Ce) is one of the most promising rare earth dopants for TiO_2 due to its exceptional redox properties. The Ce^{3+}/Ce^{4+} redox couple plays a vital role in capturing electrons and preventing their recombination with holes [21]. Ce ions introduce localized states within the bandgap, which enhances visible light absorption and shifts the absorption threshold from the UV to the visible spectrum. The presence of Cerium ions in the TiO_2 lattice also improves the charge migration process, ultimately boosting the photocatalytic activity of TiO_2 [22].

1.9 Synthesis of TiO_2 Nanoparticles

Various methods are available for synthesizing TiO_2 nanoparticles, including:

- ➢ Hydrothermal
- ➢ Sol-gel
- ➢ Mechanical milling
- ➢ Sputtering
- ➢ Solvothermal
- ➢ Chemical vapor deposition
- ➢ Laser pyrolysis
- ➢ Laser beam ablation
- ➢ Chemical etching

Among these techniques, the hydrothermal method is extensively utilized due to its straightforward process and effectiveness in synthesizing TiO_2 nanoparticles with superior properties

1.10 Eco conscious Synthesis of TiO_2 Nanoparticles Using *Piper betel* Leaves

Green synthesis has gained attention as an eco-conscious choice, sustainable, and economical method for producing titanium dioxide (TiO_2) nanoparticles. Unlike traditional chemical and physical synthesis methods, which often involve toxic solvents and harsh conditions, green synthesis utilizes plant-derived biomolecules as natural reducing and stabilizing agents [23]. This negates the necessity for deleterious chemicals and tremendously minimize the environmental threats.

Piper betel, a medicinal plant belonging to the Piperaceae family, is extensively scattered across India, Sri Lanka, Bangladesh, Taiwan, Thailand, Malaysia, and several other countries in Southeast Asia [24]. The leaves of *Piper betel* encompass a myriad of phytochemicals, for instance polyphenols, flavonoids, and alkaloids, which serve an significant role in the environmentally conscious synthesis of TiO_2 nanoparticles [24]. The extract from the leaves operates a dual capacity: it executes as a reducing agent to transform titanium precursors into nanoparticles and as a stabilizer to prevent clustering.

This process prompts nanoparticles with better biocompatibility, uniform size distribution, and enhanced photocatalytic behavior. Additionally, it is a straightforward, simple and cost-effective techniques that promotes the safe and eco-conscious manufacturing of nanomaterials.

TiO_2 nanoparticles prepared with *Piper betel* extract demonstrate significant prospect for multiple uses such as eco-conscious remediation, solar light-induced photocatalysis, and biomedical applications, due to their remarkable stability and robust efficacy [25].

1.11 Hydrothermal Method

The hydrothermal method is highly acknowledged for its efficiency in synthesizing TiO_2 nanoparticles, enabling fine-tuned regulation over their phase content and particle size [26]. This pathway operates under controlled conditions, ensuring uniform nucleation and producing nanoparticles of high purity.

The process for hydrothermal synthesis consists of the following steps:

- Preparation of the precursor solution
- Transferring the solution into an autoclave
- Heating the autoclave to the target temperature
- Allowing the system to cool congenitally
- Washing the obtained product
- Drying the material
- Grinding the dried product to get fine nanoparticles

This method also facilitates efficient doping, offering precise control over the incorporation of dopants. The result is enhanced functional properties in the synthesized nanoparticles, making them suitable for a broad range of applications, including environmental, photocatalytic, and biomedical fields.

CHAPTER 2

LITERATURE REVIEW AND METHODOLOGY

CHAPTER 2

LITERATURE REVIEW AND METHODOLOGY

2.1 Literature Review

The primary objective of this project is to effectively detoxify water tainted by pharmaceutical antibiotics. To determine the most effective pathway, an in-depth evaluation of existing literature was conducted. This involved comparing pure TiO_2 with TiO_2 doped with various elements, in addition to studying the most effective synthesis techniques for producing superior efficiency photocatalytic materials. The insights derived from these studies guided the choice of the best material composition and synthesis method, resulting in more enhanced efficiency in antibiotic degradation and comprehensive water refinement.

1. Hunagunda et al. (2017) Effectively fabricated Gd-doped TiO_2 nanoparticles using an eco-conscious method with *Piper betel* leaf extract. The addition of gadolinium (Gd) into the TiO_2 structure lead to smaller particle sizes and a significant transition in optical absorption towards the visible spectrum, effectively enhancing the photocatalytic performance of the nanoparticles. The study exhibited efficient degradation of methylene blue dye, which was attributed to improved charge separation and light absorption. Furthermore, the Gd-doped TiO_2 nanoparticles showed considerable antioxidant and antibacterial behaviour, emphasising their potential for both environmental remediation and biomedical applications.[27].

2. Sukhadeve et al. (2022) synthesized Ag and Fe co-doped TiO_2 nanoparticles using the sol-gel method to examine their versatile functionality. The study aimed at improving dopant concentrations to improve photocatalytic hydrogen generation, dye removal, and antimicrobial behaviour. Among the various tested samples, the optimized composition has gained a remarkable 80.22% degradation efficiency MB dye under visible light [28].

3. Eric Cerrato et al. (2022) Synthesized a mini-review that focused on the enhanced photocatalytic performance of TiO_2 when doped with rare earth elements like Ce, Eu, and Er, particularly for water treatment purposes. The review examines how doping with these

elements enhances light absorption in the visible range by creating intermediate energy levels within the band gap, which promotes efficient charge separation and lower the electron-hole recombination. The authors emphasize the relevance of streamlining the dopant concentrations to gain the highest photocatalytic efficiency while preserving TiO_2's crystalline structure. The review concludes that these modifications offer significant potential for real life applications in wastewater treatment, especially in enhancing the degradation of organic pollutants under visible light exposure [29].

4. Shilpy Bhullar et al. (2021) investigated an environmentally friendly pathway for synthesizing TiO_2 nanoparticles using multiple plant-based extracts, such as clove, coriander, and black pepper, was explored. The study highlighted the impact of the selected plant extracts on the size and morphology of the nanoparticles, emphasizing the role of phytochemicals in shaping the properties of the prepared materials. The TiO_2 nanoparticles revealed significant potential for therapeutic uses, indicating that green synthesis offers an eco- conscious solution [30].

5. T. Pushpamalini et al. (2021) conducted a thorough comparative study was held on the green synthesis of TiO_2 nanoparticles using extracts from four different types of leaves. The synthesized nanoparticles were rigorously assessed for their photocatalytic efficiency, specifically by measuring the degradation of malachite green dye under light irradiation. The results revealed that the choice of plant extract significantly emphasized the size, morphology, and overall photocatalytic performance of the TiO_2 nanoparticles. This signifies the pivotal role that green synthesis parameters serve in optimizing photocatalytic materials for efficient environmental remediations [31].

6. Ashwini S. Gadge et al. (2023) successfully synthesized TiO_2 nanoparticles using the sol-gel method, followed by an in-depth investigation into the impact of calcination temperature on their photocatalytic activity. The photocatalytic performance was determined using MB dye as a model pollutant. Among the various samples produced, the one calcined at the optimized temperature exhibited the highest degradation efficiency of 94.96%. This exceptional result signifies that the calcination process is essential for improving the crystallinity and photocatalytic performance [32].

7. Abel Saka and Yohannes Shifera reported an cutting-edge method for the green synthesis of TiO_2 nanoparticles using papaya shell extract. This eco-friendly approach not only facilitated the efficient formation of TiO_2 nanoparticles but also produced particles with significant antifungal properties. These results underscore the dual potential of the nanoparticles for both biological and environmental applications.[33].

8. **Ashwini S. Gadge et al. (2024)** reported the successful green synthesis of Ce-doped TiO_2 nanoparticles, resulting in significantly improved photocatalytic activity, along with antibacterial properties and a highly hydrophilic self-cleaning surface. The incorporation of cerium into the TiO_2 lattice was found to be essential in enhancing charge separation and optimizing surface properties. These modifications led to a material that performs outstandingly under visible light, making it ideal for multiple applications. The multifunctional characteristics of Ce-doped TiO_2 make it a strong contender for environmental remediation, particularly in water purification, self-cleaning coatings, and antimicrobial surfaces [34].

9.**Khozema Ahmed Ali et al. (2017)** explored the photocatalytic capabilities of cerium and lanthanum co-doped TiO_2 nanoparticles for CO_2 reduction under visible light. The results showed that the addition of cerium considerably improved the material's absorption of visible light and overall photocatalytic performance. By methodically determining the effects of different Ce doping levels, they demonstrated that optimal doping concentrations are essential for enhancing charge separation and promoting the CO_2 reduction process [35].

10.M. Nasir et al. (2014) reported the synthesis of TiO_2 nanoparticles co-doped with Ce and N using a hydrothermal technique to enhance their photocatalytic efficiency under visible light. The co-doping of a metal and a non-metal resulted in a noticeable reduction of the band gap, which enhanced the visible light absorption and facilitated better charge carrier separation. These advancements led to a substantial enhancement in the photocatalytic degradation of pollutants. Their study demonstrates how the combination of metal and non-metal dopants can effectively modify the optical and electronic properties of TiO_2, a path way for the development of advanced photocatalysts for environmental remediation [36].

11.H. Liu et al. (2011) synthesized mesoporous CeO_2–TiO_2 nanoparticles using an groundbreaking ionic liquid-templated method. The mesoporous nanocomposites revealed excellent photocatalytic performance under both UV and visible light irradiation. This enhancement was attributed to the mesoporous structure, which offered a high surface area and enhanced light absorption. Additionally, the collaborative effect between CeO_2 and TiO_2 promoted more significant charge carrier separation and minimized recombination rates. This study highlights the significance of template-assisted nano structuring and heterojunction formation in developing enhanced photocatalysts for environmental remediation and ecofriendly energy applications [37].

2.2 Objective

A comprehensive survey of current studies emphasizes the major environmental hazards linked to pharmaceutical antibiotics such as ciprofloxacin. Ciprofloxacin poses a serious threat to the environment, particularly aquatic ecosystems. A detailed survey of current research signifies this increasing apprehension and identifies photocatalysis as a feasible approach. This technique stands out for its ability to effectively and sustainably break down toxic substances.

TiO_2 is one of the most well-examined photocatalysts but it has some drawbacks. To address the challenges of TiO_2, researchers have turned to doping TiO_2 with rare earth elements such as cerium. Cerium helps to introduce new energy levels within the band gap and creates surface traps, both of which improve visible light absorption and minimize charge recombination, resulting in enhanced photocatalytic activity.

In recent years, green synthesis methods have acquired attraction as they are environmentally safe. Despite the fact that several studies have explored rare earth-doped TiO_2, there is minimal studies on Ce-doped TiO_2 nanoparticles synthesized through green hydrothermal methods for degradation of ciprofloxacin.

This project concentrates on tackling that shortcoming. The primary objective is to synthesize, chracterize and analyze Ce-doped TiO_2 nanoparticles using a green route via hydrothermal pathway and tested for ciprofloxacin degradation under visible light irradiation.

The project is hence titled as: "**Synthesis and Characterization of Ce-doped TiO_2 Nanoparticles for Pharmaceutical Antibiotic Degradation.**"

2.3 Methodology

The project followed a methodological and multi-dimensional pathway.

1. Synthesis:

Pure TiO_2 and Ce-doped TiO_2 nanoparticles were synthesized via an eco-friendly green hydrothermal process, utilizing plant-based extracts to promote sustainability and control over particle properties.

2. Characterization Techniques:

The synthesized samples underwent comprehensive physicochemical and structural analyses, including:

- ➢ TGA and DTA study
- ➢ X-ray Diffraction spectroscopy (XRD)
- ➢ Raman Spectroscopy
- ➢ SEM and EDS analysis
- ➢ FTIR analysis
- ➢ UV-Vis Spectroscopy
- ➢ Photoluminescence analysis

3. Photocatalytic Performance Evaluation:

The photocatalytic performance of all samples was assessed by monitoring the decomposition of ciprofloxacin under visible light exposure, providing insights into their potential for real-world wastewater treatment applications.

CHAPTER 3
SYNTHESIS OF MATERIAL AND CHARACTERIZATION TECHNIQUES

CHAPTER 3
SYNTHESIS OF MATERIAL AND CHARACTERIZATION TECHNIQUES

3.1 Synthesis of Materials

3.1.1 Materials and Reagents

Titanium tetraisopropoxide (TTIP, 97% purity, Sigma-Aldrich) served as the titanium precursor for synthesis. Ethanol (99.9%, analytical grade), obtained from Hongsheng Fine Chemical Co. Ltd., was used as the solvent. Cerium nitrate hexahydrate [$Ce(NO_3)_3 \cdot 6H_2O$] and ciprofloxacin employed as the model pharmaceutical pollutant were purchased from Alfa Aesar. All solutions were prepared with double-distilled water to ensure maximal purity. Every chemical and reagent used was of analytical grade and utilized directly without any further purification steps.

3.1.2 Synthesis of Cerium Doped TiO_2 Nanoparticles

An environmentally sustainable hydrothermal technique was employed to synthesize cerium-doped TiO_2 nanoparticles, aligning with green chemistry principles. Cerium (Ce) was introduced at various molar concentrations of 0%, 0.3%, 0.5%, 0.7%, and 0.9%—to systematically examine its effect on photocatalytic activity. The resulting samples were distinctly labeled according to their respective doping levels, as outlined in Table 3.1. This green synthesis strategy enabled precise control over nanoparticle crystallization while minimizing environmental impact, promoting a clean and sustainable production process.

Preparation of Leaf Extract

The synthesis process began with the preparation of a leaf extract from *Piper betel* leaves. The leaves were thoroughly cleaned with double-distilled water and then dried at room temperature for several hours. Following this, 20 grams of chopped leaf pieces were heated at 70°C for 45 minutes in 200 ml of distilled water while stirring continuously. After cooling to room temperature, the extract was filtered using Whatman filter paper to obtain a clear solution.

Synthesis of Ce-Doped TiO_2

1. Preparation of Solution A: To prepare Solution A, 9 ml of titanium tetraisopropoxide (TTIP) was added dropwise to 45 ml of the prepared leaf extract, and the mixture was stirred for 10 minutes to ensure homogeneity.

2. Preparation of Solution B: Solution B was prepared by dissolving the desired concentration of cerium nitrate hexahydrate ($Ce(NO_3)_3 \cdot 6H_2O$) in 50 ml of distilled water, followed by stirring for 5 minutes.

3. Combination of Solutions: Solution B was then added dropwise to Solution A while stirring continuously. The resulting mixture was stirred for an additional 45 minutes to achieve a homogeneous colloidal solution.

4**. Hydrothermal Treatment:** The acquired brown-colored colloidal solution was poured into an autoclave and heated in an oven set at 170°C for 3 hours. After the hydrothermal process, the solution was left to cool naturally to room temperature.

5. Centrifugation and Drying: The prepared solution were centrifuged several times with ethanol and distilled water to eliminate any impurities. The purified nanoparticles were then placed in an oven to dry at 80°C overnight.

6. Calcination: Finally, the dried sample was calcinated at 500°C for 2 hours to enhance its crystallinity and photocatalytic properties.

Fig.3.1 Synthesis of Ce doped TiO_2 nanoparticles by hydrothermal method using green synthesis

All samples were prepared under the same conditions to ensure consistency in the synthesis process. A schematic diagram illustrating the entire synthesis process is provided in Fig. 3.1.

Table 3.1 Identifications of prepared photocatalysts

Sample Code	Doping Status
CeT_0	TiO_2 in its pure form
CeT_0.3	Cerium-doped TiO_2 containing 0.3 mol% Ce
CeT_0.5	Cerium-doped TiO_2 containing 0.5 mol% Ce
CeT_0.7	Cerium-doped TiO_2 containing 0.7 mol% Ce
CeT_0.9	Cerium-doped TiO_2 containing 0.9 mol% Ce

3.2 Characterization Techniques

Some techniques were used to analyze thermal properties, crystallinity, surface morphology, optical properties, etc. The techniques are: -

➢ TGA-DTA study

➢ X-Ray diffraction spectroscopy

➢ Raman spectroscopy

➢ FTIR analysis

➢ SEM analysis

➢ UV-Vis spectroscopy

➢ Photoluminescence analysis

3.2.1 TGA-DTA study

Thermogravimetric analysis (TGA) is a crucial method for evaluating the thermal stability of materials by examining the variation in weight as temperature increases at a constant rate, providing valuable information about the various components present in the sample. A thermogravimetric analyzer, as depicted in Fig. 3.2.

Fig. 3.2 HITACHI STA7200

consists of a balanced sample holder (pan) housed within a controlled furnace. The resulting data forms a **TGA curve,** where the x-axis indicating temperature or time, and the y-axis shows the percentage of mass loss or the absolute mass. In the TGA curve, a stable sample will exhibit no mass change at specific temperatures, while a gentle slope indicates negligible mass loss, reflecting ongoing stability. TGA identifies the upper temperature limit of a sample, beyond which material degradation begins. Additionally, derivative thermogravimetric analysis (DTG) enhances this assessment by illustrating the rate of weight change relative to temperature; its plot features temperature along the x-axis and the rate of weight change along the y-axis, allowing for a more detailed understanding of thermal transitions and decomposition behavior [38].

3.2.2 X-Ray diffraction spectroscopy

X-ray diffraction (XRD) is an essential technique used to analyze the crystalline structure and atomic spacing of materials, allowing for the analysis of both bulk and non-bulk structures, including nanoparticles and metastable phases in bulk materials, thereby revealing new physical properties. This technique operates on the principle of constructive interference that occurs between monochromatic X-rays and a crystalline material. X-rays are generated by a cathode ray tube, filtered to produce monochromatic radiation, collimated to focus the beam, and directed onto the sample. The crystalline substance acts as a three-dimensional diffraction grating for the X-rays. In an X-ray diffractometer, the sample is rotated at an angle (θ) relative to the collimated X-ray beam, while the X-ray detector rotates at an angle of (2θ) to capture the diffracted X-rays. A goniometer is employed to maintain the angle and facilitate the rotation of the sample.

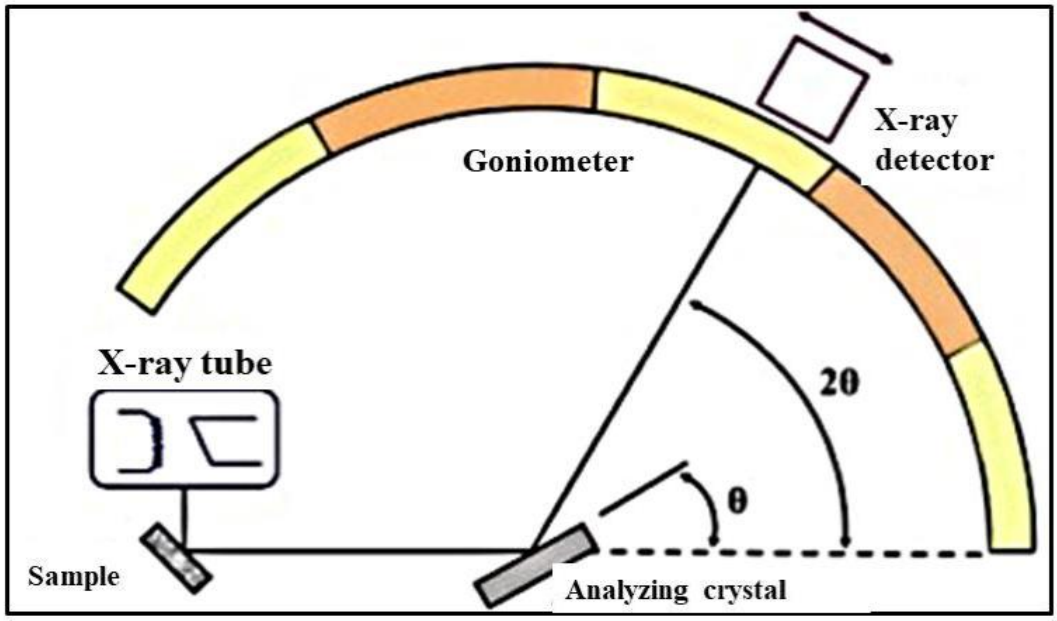

Fig. 3.3 Schematic diagram of X-ray diffractometer

According to Bragg's law, constructive interference—and subsequently, the generation of a diffracted ray—occurs when the X-rays impinge on the sample. This relationship can be expressed with the equation

$$n\lambda = 2dsin\theta \qquad \text{eq. (3.1)}$$

where (n) represents an integer, (λ) signifies the X-ray wavelength, (d) refers to the interplanar spacing contributing to the diffraction, and (θ) denotes the angle of diffraction. This fundamental principle links the wavelength of electromagnetic radiation to both the diffraction angle and the lattice spacing within a crystal. The diffracted X-rays are subsequently detected, processed, and analyzed over a range of (2θ) angles, allowing for the identification of all possible lattice diffraction directions due to the arbitrary alignment of powdered material. The identity of the compound can be established by comparing the observed diffraction peaks to the corresponding d-spacing values, as each compound possesses a unique set of d-spacing parameters, typically referenced against databases such as the JCPDF files.

When interpreted accurately, the XRD pattern provides a characteristic "fingerprint" of the crystalline phases present in the sample, enabling the identification of crystalline forms. Additionally, it is possible to determine the crystalline size and strain by analyzing the broadening of spectral lines. For crystallite size estimation, Scherrer's formula is utilized, expressed as follows:

$$D = \frac{k\lambda}{\beta cos\theta} \qquad \text{eq. (3.2)}$$

where (D) stands for the crystallite size, (K) represents the shape factor (usually 0.9 for most samples), (λ) signifies the X-ray wavelength, (β) denotes the full width at half maximum (FWHM) in radians, and (Θ) corresponds to the Bragg diffraction angle [39].

Fig. 3.4 D8 quest system (Bruker diffractometer)

The XRD analysis for all samples was conducted using the D8 Quest system from Bruker diffraction, as illustrated in Fig. 3.4 This comprehensive assessment of XRD patterns not only provides insights into the crystalline structure but also enhances the understanding of the material's physical characteristics.

3.2.3 Raman Spectroscopy

Raman spectroscopy is a reliable and non-intrusive analytical method widely used to study phonons in solids, liquids, and gases. It delivers essential insights about material phases and physical processes like spin-phonon coupling, electron-phonon interactions, orbital-lattice dynamics, and phase transitions. The technique works by examining the inelastic scattering of monochromatic light, generally sourced from a laser. When this light comes into contact with a material, the frequency of the scattered light changes, indicating the presence of the Raman effect. The material absorbs the incident light and re-emits it, with the resulting frequency shift reflecting the molecular vibrations, rotations, and low-energy transitions of the material.

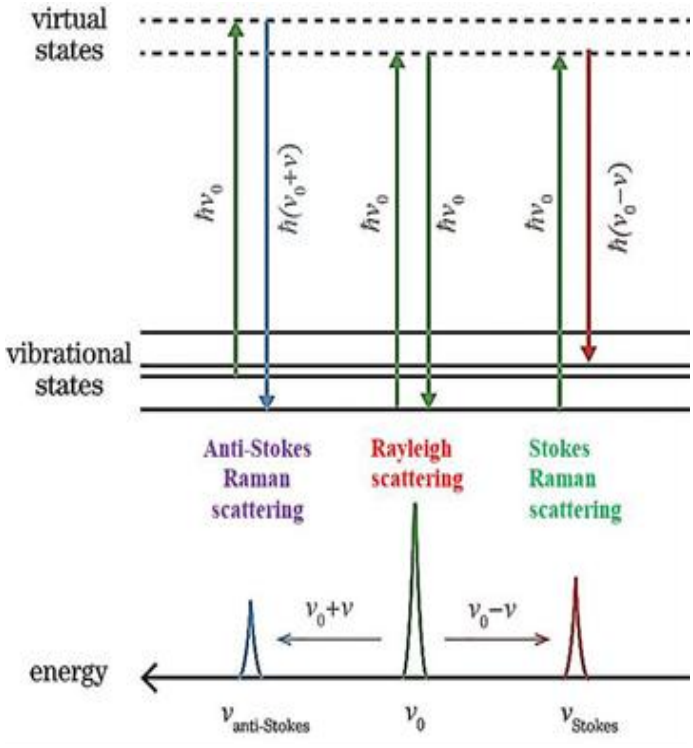

Fig 3.5 Schematic representation of energy states participating in Raman spectroscopy

The Raman effect arises from changes in molecular polarizability (α), which occur when a molecule is distorted by an electric field. The electric dipole moment is given by ($P = \alpha E$), where (E) is the electric field of the laser light, resulting in repeated molecular deformation and vibration at the molecule's characteristic frequency. When the molecule returns to its ground state, it emits radiation at three distinct frequencies, as illustrated in the energy level diagram (Fig. 3.5).

These include Rayleigh scattering, where there is no change in the vibrational state and the scattered light retains the same frequency as the incident light, and Stokes scattering, which takes place when the molecule absorbs energy and transitions to a higher vibrational state, resulting in scattered light with a lower frequency. Conversely, Anti-Stokes scattering happens when the molecule, already in an excited vibrational state, interacts with the laser and gains additional energy, emitting light at a higher frequency [40]. In this study, Raman spectroscopy was conducted at room temperature using a HEDA-URSM4/5/7 instrument (Fig. 3.6) with a 532 nm laser as the excitation source.

Fig. 3.6 Experimental setup of NOST: HEDA-URSM4/5/7 Raman spectrometer

3.2.4 FTIR (Fourier Transform Infrared) Spectroscopy

FTIR (Fourier Transform Infrared) spectroscopy is a valuable technique used to investigate the functional groups and chemical bonding within materials. This technique is reliant on

the absorption of infrared radiation by a sample, which prompts molecular vibrations such as stretching and bending of chemical bonds. As infrared light interacts with the sample, certain wavelengths are absorbed, provoking vibrations that match specific energy levels. The absorption spectrum produced serves as a distinct vibrational fingerprint of the material, facilitating the recognition of various chemical bonds and functional groups within the sample [47].

FTIR functions by recording high-resolution spectral data across a wide range of wavelengths using an interferometer, which then applies a mathematical Fourier transform to transmute the raw data into an absorption spectrum for straightforward interpretation. In this study, FTIR spectra were documented using a JASCO FTIR-4600 spectrometer with a measurement range of 400–4000 cm^{-1}. This analysis provided crucial facts about the functional groups in the materials, confirming the successful synthesis and interaction of sample components. It also underscored the light-harvesting properties of photocatalysts and their potential applications in fields like dye degradation and environmental restoration.

Fig.3.7 JASCO FTIR-4600 spectrometer

3.2.5 Scanning Electron Microscopy (SEM)

Scanning Electron Microscopy (SEM) is a cutting-edged technique used to closely scrutinize the surface structure of materials. It works by directing a finely focused electron beam over the material's surface and detecting the signals produced when the beam interacts with the atoms of the sample. The electron beam is generated either through field emission or from a heated filament, and it is focused and accelerated by electromagnetic lenses to safeguard the beam is directed with meticulousness onto the sample. The schematic diagram of the SEM setup is illustrated in Fig. 3.8. As the electron beam strikes the specimen, various signals are emitted, including secondary and backscattered electrons, along with characteristic X-rays. SEM primarily detects secondary electrons to create high-resolution visuals that expose intricate surface features at the nano range. The spatial distribution and intensity of these signals are captured by specialized detectors and processed into detailed images using advanced computer algorithms.

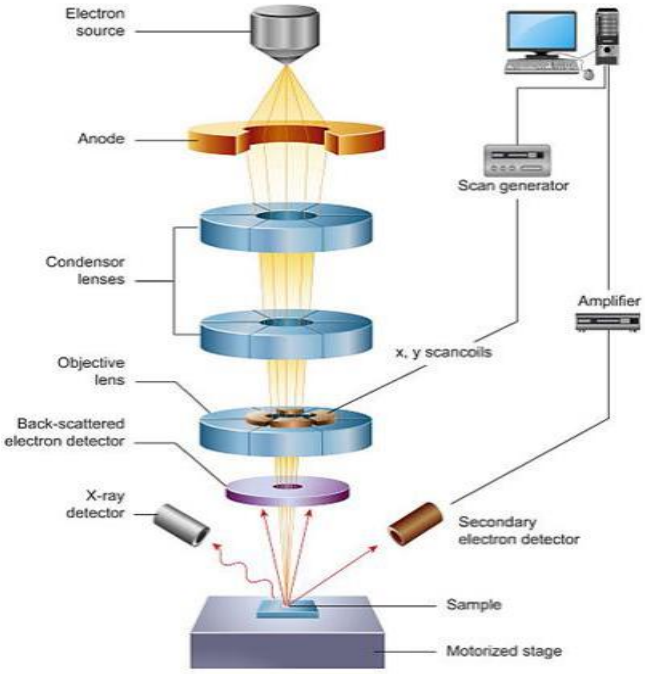

Fig. 3.8 Experimental setup of SEM

SEM allows for in-depth surface characterization with magnifications reaching up to millions of times, surpassing the capabilities of traditional optical microscopes. This enables visualization of complex surface textures and microstructures with remarkable clarity [41]. Furthermore, due to its non-destructive nature, SEM is particularly suited for

the analysis of delicate materials without causing damage. In this study, all SEM images were obtained utilizing the “ZEISS Evo SEM18” instrument, with the experimental setup and schematic of the device shown in the corresponding Fig. 10.

Fig. 3.9 Schematic representation of ZEISS evo SEM18, SEM instrument

3.2.5.1 Energy-dispersive X-ray spectroscopy (EDS or EDX)

Energy-dispersive X-ray spectroscopy is a sophisticated analytical technique used to determine the elemental composition of a sample. It works by directing an intensified electron beam onto the surface of the sample, exciting the atoms in the focused region. As these excited atoms return to their ground state, they emit X-rays that are characteristic of each element.

The emitted X-rays are collected by an X-ray detector, and the resulting signals are analyzed to determine which elements are present in the sample. EDS is capable of detecting elements from carbon to uranium, including trace elements as small as 1.0 wt%. When paired with a scanning electron microscope (SEM), EDS offers precise, localized elemental analysis, enabling the study of elemental distribution in specific microscopic regions.

The fundamental aspects of an EDS system include:

- **X-ray Detector**: Captures the X-rays emitted from the sample.

- **Pulse Processor**: Converts the X-ray signals into voltage pulses that correspond to their energy levels.
- **Computer**: Processes these pulses to create an energy spectrum, which provides qualitative and quantitative data about the sample's elemental composition.

This combination of technologies facilitates detailed, instant elemental analysis with fine spectral resolution at the microscopic scale.

3.2.6 UV-Visible Spectroscopy

This non-invasive method depends on the absorption of UV and visible light by electrons in a material, which induces electronic transitions between energy levels. When a material is exposed to light in the UV-Visible range (typically 200–800 nm), electrons in the valence band may absorb energy and migrate to higher energy states, such as the conduction band. The amount of light absorbed at different wavelengths is measured and recorded as an absorption spectrum. The position and intensity of the absorption peaks yield crucial information about the electronic transitions and band structure of the material.

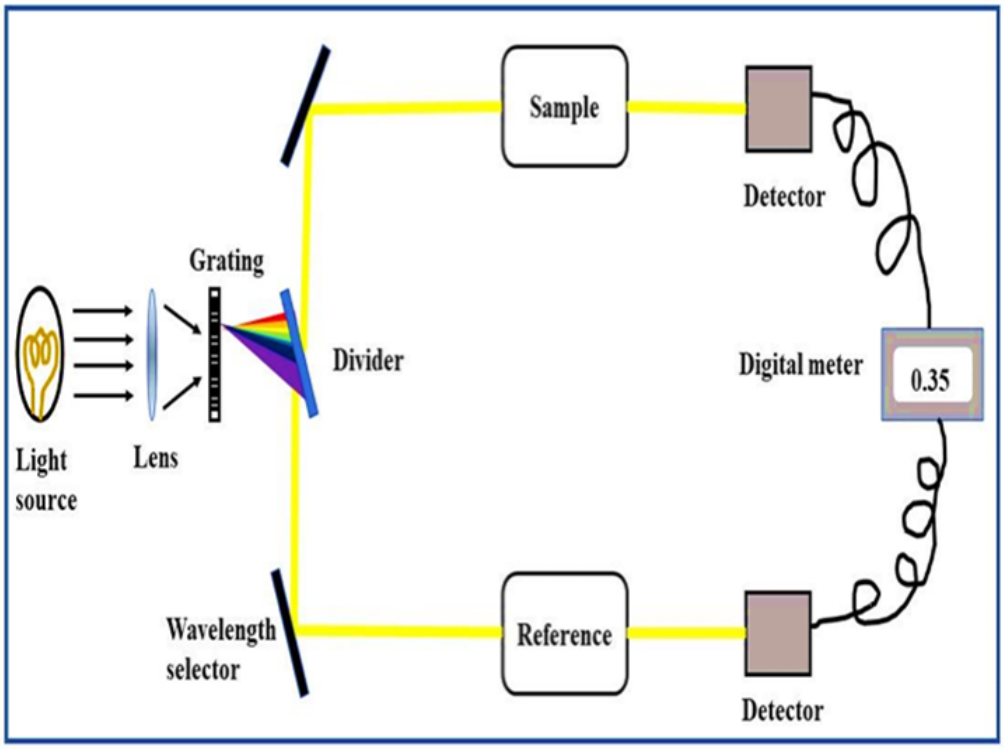

Fig. 3.10 Ray-diagram of double beam spectrophotometer

For semiconducting materials like TiO_2, UV-Visible spectroscopy is particularly advantageous for assesing the band gap energy E_g. The optical band gap is defined as the minimum energy requisite to excite an electron from the valence band to the conduction band. This energy can be calculated using Tauc's relation, which connects the absorption coefficient (α) to photon energy ($h\nu$):

$$(\alpha h\nu)^n = A(h\nu - E_g) \qquad \text{eq. (3.3)}$$

The absorption coefficient is denoted by (α), photon energy is represented as (hν), (A) is a constant, E_g is the optical band gap, and (n) is dependent on the type of electronic transition (with n=1/2) for direct allowed transitions and (n = 2) for indirect allowed transitions. By plotting $(\alpha h\nu)^n$ versus $(h\nu)$ (known as a Tauc plot) and extrapolating the linear portion of the curve to the photon energy axis, the band gap energy can be deduced. In this project, the UV-Visible absorption spectra of the prepared samples were recorded using a JASCO V-750 UV-Visible spectrophotometer over the range of 200 to 800 nm. The optical absorption edge and corresponding band gap values were determined from the Tauc plots, and shifts in the absorption edge can indicate the effects of doping, crystallite size, or structural defects within the material [45][46].

Fig. 3.11 JASCO V-670, UV-Vis-NIR spectrophotometer

3.2.7 Photoluminescence Spectroscopy

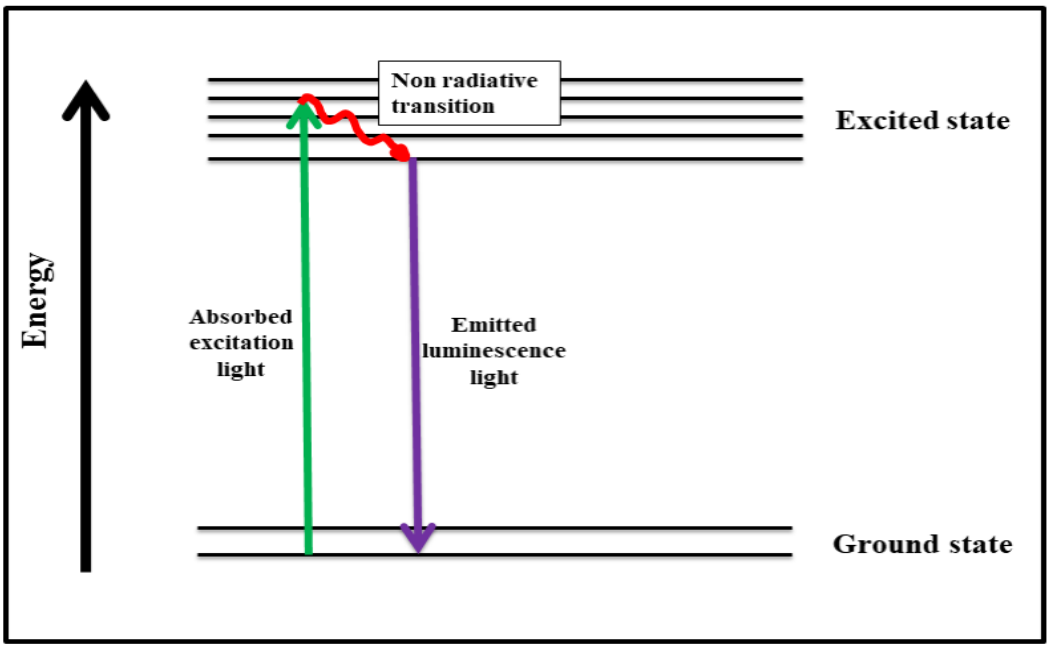

Fig. 3.12 Energy level diagram for electronic transition

Photoluminescence (PL) spectroscopy is a non-invasive optical technique instrumental for investigating the electronic structure of materials. This method involves exposing a material to high-energy light, which excites electrons to higher energy states. As these excited electrons transition back to their ground state, they emit light known as photoluminescence. The process includes radiative relaxation, where electrons emit photons with energies that correspond to the material's electronic transitions. Emission happens due to the recombination of charge carriers created during the excitation process. Photoluminescence is broadly categorized into two types: fluorescence, characterized by a rapid relaxation process occurring within (10^{-8} to 10^{-5}) seconds, and phosphorescence, which involves a slower relaxation process that can take significantly longer. The spectral intensity and energy profile of the emitted light offer valuable insights into the material's properties, including its electronic structure, bandgap, defects, and impurities. An energy level diagram (Fig. 3.12) effectively illustrates the PL process. At room temperature, electrons are typically in the ground state. When the material absorbs energy from incident photons, electrons are promoted to higher, unstable energy states, which encompass multiple vibrational sublevels. Initially, some energy is lost through non-radiative relaxation as the electron transitions to a lower vibrational level within the excited state. Ultimately, the electron transitions radiatively to the ground state, emitting a photon with

energy ($E = h\nu$), which aligns with the energy gap between the starting and ending energy states. This emitted photon typically falls within the visible light range, characterizing photoluminescence.

Fig. 3.13 JASCO FP-8200 Spectroflurometer

In this study, the emission spectra of the prepared samples were measured using a JASCO FP-8200 spectrofluorometer (Fig. 3.13). This instrument comprises an excitation source, a sample holder (cuvette), and a fluorescence detector. Excitation is provided by a shielded Xenon lamp covering a wavelength range of 200–750 nm. The broadband radiation undergoes filtering through a monochromator to isolate a specific wavelength for excitation. The resulting fluorescence is subsequently filtered through another monochromator and detected by a photomultiplier tube. In semiconductors, photoluminescence often involves electron transitions between the conduction and valence bands, with the emitted energy corresponding to the material's bandgap. PL studies not only help estimate the bandgap but also reveal information about defect states, impurity levels, and the recombination mechanisms of excited charge carriers [43][44].

CHAPTER 4

RESULTS AND DISCUSSION

CHAPTER 4

RESULTS AND DISCUSSION

4.1 TGA-DTA Study

To investigate the thermal properties—including decomposition behavior, phase transitions, thermal stability, and reaction kinetics, thermogravimetric analysis (TGA) and differential thermal analysis (DTA) were conducted **(Fig. 4.1).** The TGA curve revealed three distinct stages of weight loss:

1. First stage: Attributed to the evaporation of physically adsorbed surface water, accounting for an 11.62% reduction in weight.
2. Second stage: Corresponding to the decomposition of residual organic solvents, resulting in an additional 8.43% weight loss.
3. Third stage: Associated with structural transformation from an amorphous to a crystalline phase [38], exhibiting a minimal weight loss of 0.5%.

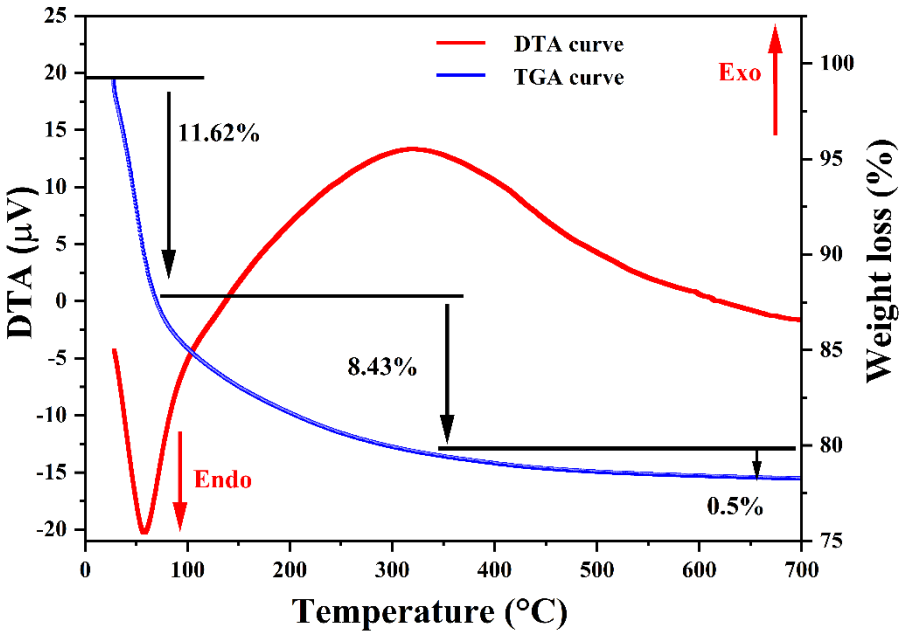

Fig. 4.1 TGA-DTA curves of synthesized samples

In the DTA curve, an endothermic peak observed around 55 °C indicates the evaporation of physically bound water and solvent molecules. Furthermore, a broad exothermic peak near 327 °C signifies the crystallization process of the material [48]. These thermal events,

clearly depicted in the accompanying graph, highlight key transitions and the thermal stability profile of the material—fundamental insights essential for understanding its performance and durability under heat stress.

4.2 XRD Analysis

The X-ray diffraction (XRD) patterns of the synthesized nanoparticles are illustrated in **Fig. 4.2,** recorded over a 2θ range of 20° to 80°. All observed diffraction peaks are characteristic of the anatase phase of TiO_2, with the most intense peak appearing at 2θ = 25.3°, which corresponds to the standard reference JCPDS card no. 21-1272. Notably, no distinct peaks related to Ce doping were identified, potentially due to either the low concentration of the dopant or the successful incorporation of Ce ions into the TiO_2 lattice. Furthermore, the broadening of the diffraction peaks indicates that the samples are composed of very small nanocrystals, reflecting high crystallinity at the nanoscale [49].

The crystallite size was calculated using S**cherrer's formula** and summarized in **Table 4.1.**

$$D = \frac{k\lambda}{\beta cos\theta} \qquad \text{eq. (4.1)}$$

where:

(D) = average crystallite size (in nm),

(λ) = X-ray wavelength (1.5406 Å for Cu-Kα radiation),

(K) = shape factor (typically taken as 0.9),

(β) = full width at half maximum (FWHM) in radians,

(Θ) = Bragg diffraction angle.

Table 4.1 Calculated average crystallite size of all synthesized nanoparticles

Sample ID	Crystallite Size (nm)
CeT_0	**8.4622**
CeT_0.3	**8.6526**
CeT_0.5	**8.4204**
CeT_0.7	**8.4469**
CeT_0.9	**8.0642**

A detailed analysis of the X-ray diffraction (XRD) spectra indicated that as cerium doping concentration increased from 0.3 to 0.9 mol%, the characteristic anatase peaks became broader and exhibited reduced intensity, reflecting a decrease in the strength of Ti–O bonding and a decline in the overall orderliness of the TiO_2 crystal structure [50][51][21]. Notably, the prominent anatase (101) diffraction peak showed a systematic shift toward lower 2θ angles (Fig. 4.2). This shift is attributed to the ionic radius mismatch between Ti^{4+} (0.068 nm) and the larger dopant ions Ce^{4+} (0.101 nm) and Ce^{3+} (0.111 nm), providing strong evidence for the successful incorporation of cerium into the TiO_2 crystal lattice [21][22]. The substitution of Ti^{4+} with larger Ce ions results in lattice distortion and likely promotes the formation of oxygen vacancies, which further alters the structural framework of the TiO_2 matrix. These modifications have significant implications for the material's crystallographic properties and its photocatalyt*ic performance.*

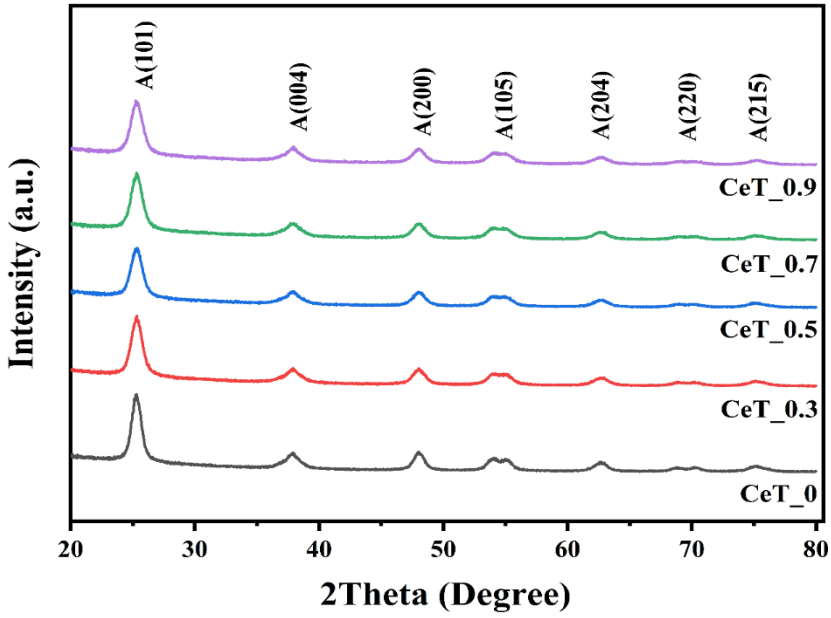

Fig. 4.2 XRD of prepared samples

4.3 Raman Analysis

The structural validation of the synthesized nanoparticles was further confirmed by Raman spectroscopy, conducted at room temperature using a 532 nm laser **(Fig. 4.3)**. Based on factor group analysis, all detected Raman bands correspond to six Raman-active modes categorized as (A_{1g}+2B_{1g}+3E_g). These modes were clearly observed, with the dominant peak appearing at 144 cm^{-1}, which is indicative of the anatase phase of TiO_2. Additional characteristic peaks of the anatase phase were recorded at 397 cm^{-1}, 522 cm^{-1}, and 639

cm^{-1}, corresponding to the symmetric bending B_{1g}, anti-symmetric bending A_{1g}, and symmetric stretching E_g vibrations of the O–Ti–O bonds, respectively [52]. Importantly, no signals associated with other TiO_2 phases or impurities were detected, reinforcing the findings from the XRD analysis. Furthermore, the spectra showed that as the doping concentration increased, the Raman peaks became broader and their intensity diminished. This behavior is attributed to structural distortion resulting from the incorporation of Ce ions into the TiO_2 lattice and a concomitant reduction in crystallite size [53].

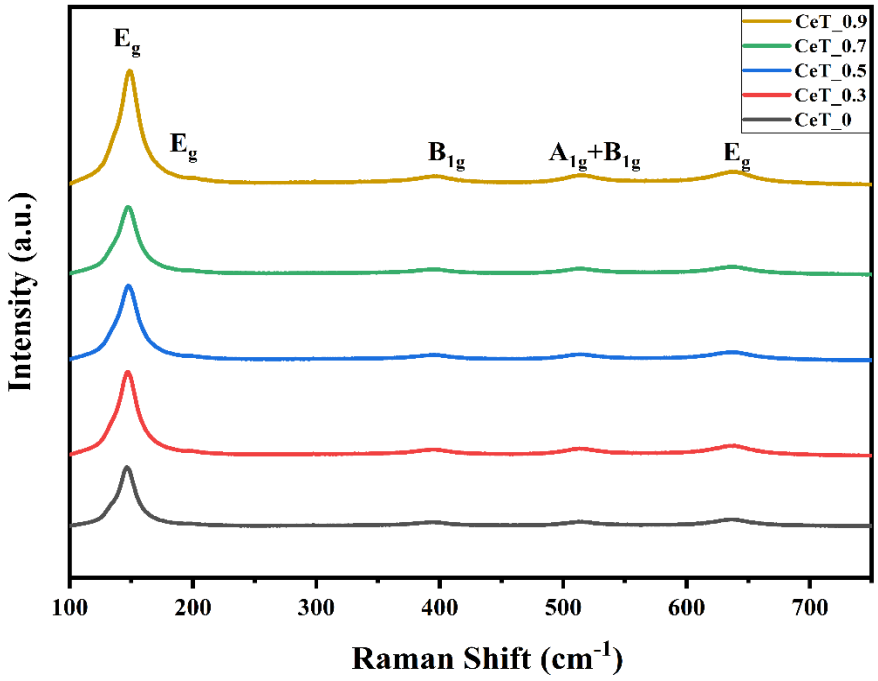

Fig. 4.3 Raman spectra of synthesized samples

4.4 FTIR Analysis

FTIR spectroscopy was employed to analyze the chemical bonds and functional groups present in the synthesized samples. As depicted in **Fig. 4.4,** the spectra were recorded over the wavenumber range of 500–4000 cm^{-1} for all samples.

A absorption band observed between 3500–3720 cm^{-1} linked to the O–H stretching vibrations of surface-adsorbed water molecules [54]. Notably, the intensity of this band increases progressively with higher cerium doping levels, indicating an increased abundance of hydroxyl groups present on the TiO_2 surface. This enhancement suggests that cerium incorporation facilitates the attachment of hydroxyl groups to the TiO_2 surface, which is instrumental in promoting photocatalytic activity. Additionally, a distinct peak

within the 1500–1600 cm^{-1} range is attributed to the bending vibrations of molecular water (H–O–H) adsorbed on the surface [55][21]. Several intense absorption bands appearing below 900 cm^{-1} are associated with the stretching vibrations of Ti–O–Ce and Ti–O bonds, confirming the successful integration of cerium into the TiO_2 lattice and the formation of heterometallic Ti–O–Ce linkages [56].

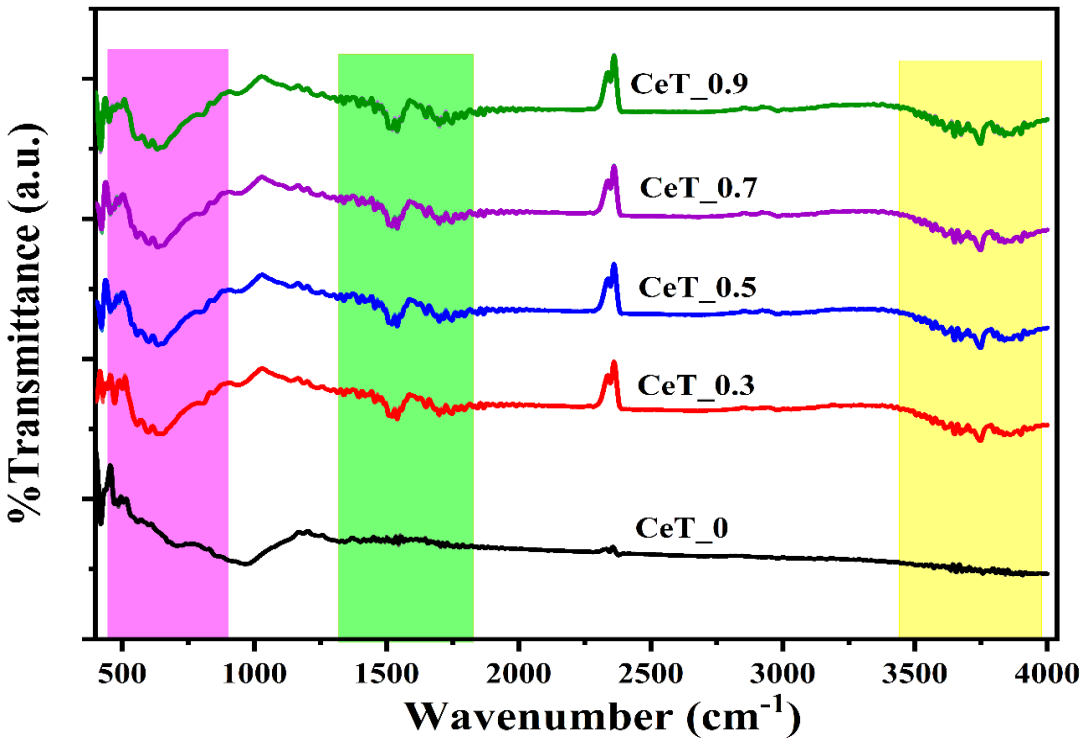

Fig. 4.4 FTIR of prepared samples

4.5 SEM Analysis

To examine the surface morphology of prepared samples, SEM analysis was conducted and depicted in Fig. 4.5((a)-(g)). From the figure, it is found that particles have a non-uniform spherical shape, and less agglomerated on increasing doping content resulting in a size reduction of particles [53][57]. Elemental composition was checked by an EDS study (fig. 4.5 (f)). The identification of Ti, O, and, Ce without any impurities in prepared samples confirms the purity and successful synthesis of prepared samples. The elemental mapping of Ti, O, and, Ce is shown in Fig. 4.4 (f), which reveals a small amount of Ce evenly distributed all over the TiO2 surface.

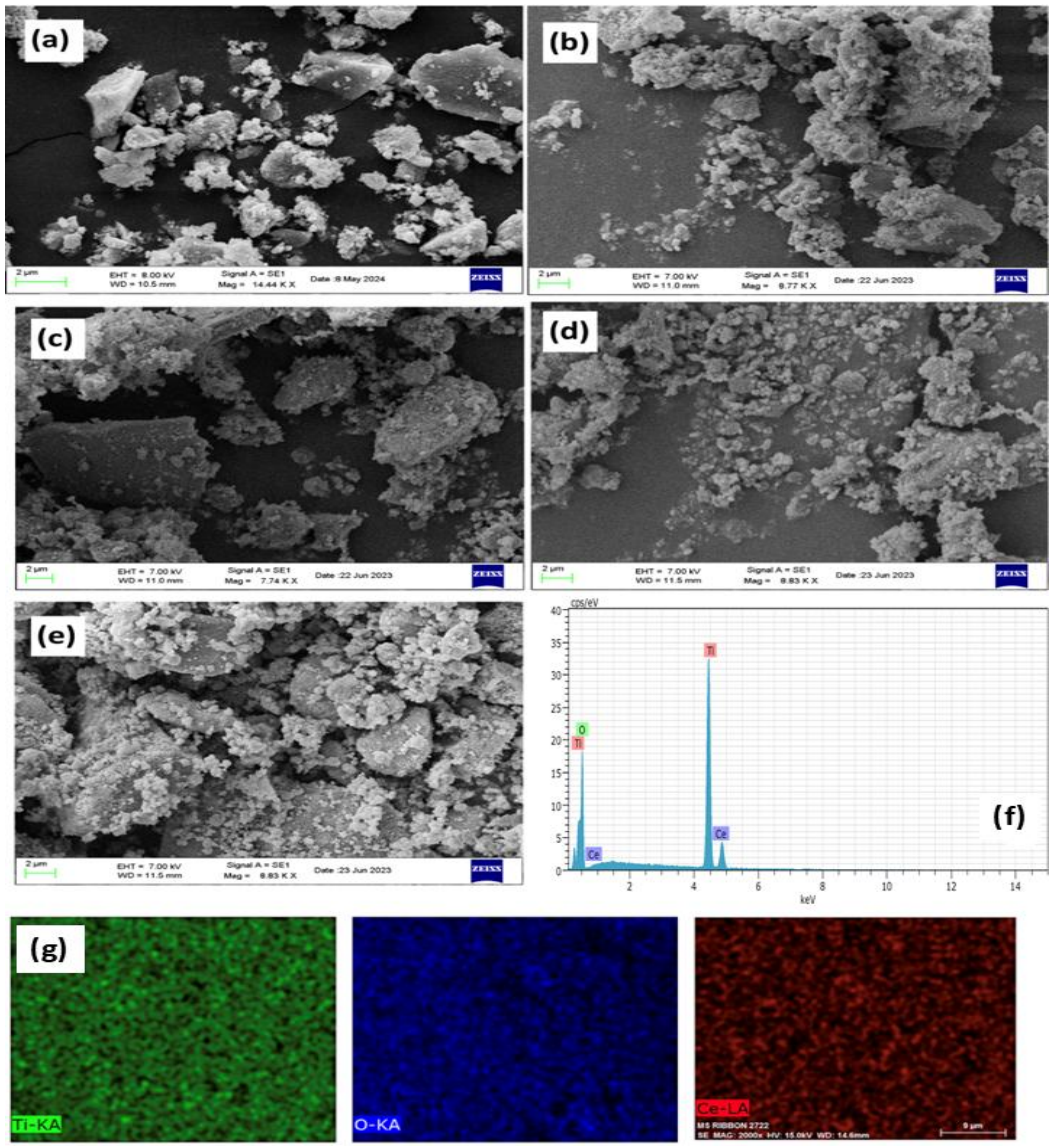

Fig. 4.5 Surface morphology of (a) CeT_0, (b) CeT_0.3, (c) CeT_0.5, (d) CeT_0.7, (e) CeT_0.9 and (f) EDS, and (g) elemental mapping of CeT_0.9

4.6 UV-Vis Analysis

The UV-Vis spectra, displayed in Fig 4.6, were recorded to investigate the optical properties of the synthesized samples. The optical absorption behavior of Ce-doped TiO_2 photocatalysts was examined within the wavelength range of 250–600 nm. The data indicate that the absorption edges of the Ce-doped TiO_2 samples exhibit a minor redshift toward the visible region compared to pure TiO_2. This shift is ascribed to a charge transfer

transition between the Cerium's 4f electrons and the valence or conduction bands of TiO_2 [58], suggesting modifications in the electronic structure due to doping.

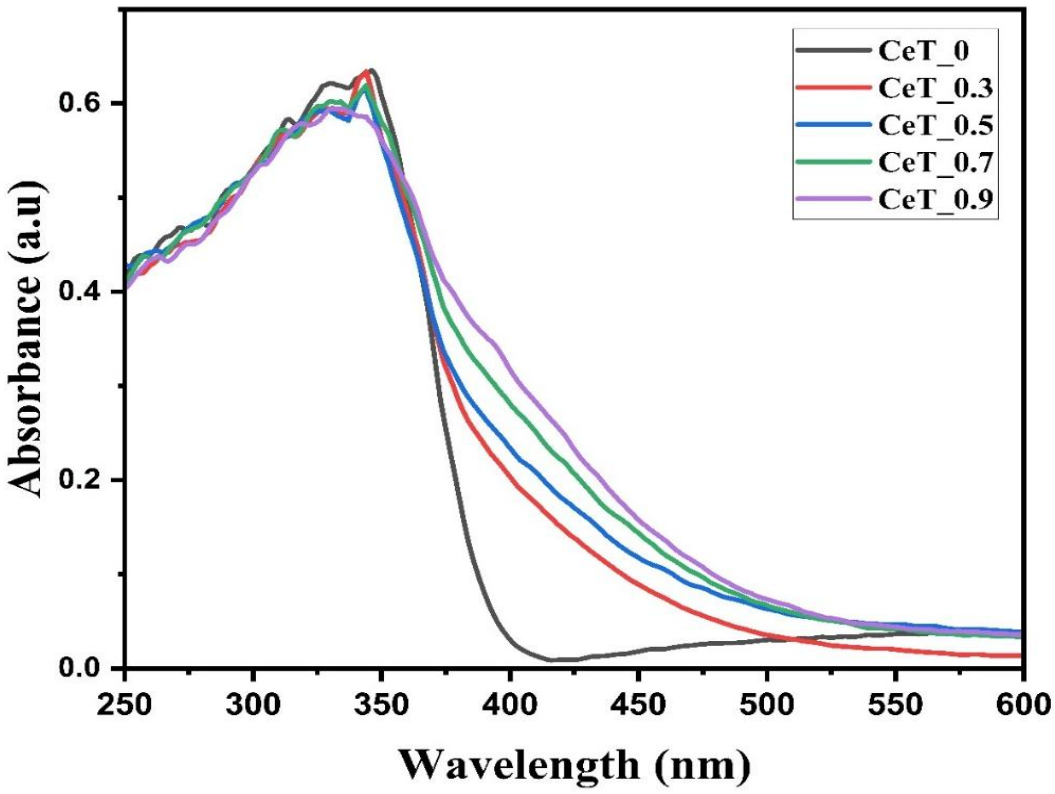

Fig. 4.6 UV-Vis spectra of prepared samples

The energy band gap E_g was determined using Tauc's plot (Fig. 4.7), represented by the following equation:

$$(\alpha h\nu)^n = A(h\nu - E_g)\ , \qquad \text{eq. (4.2)}$$

Where:

E_g = energy band gap,

$h\nu$ = photon energy,

α = absorption coefficient,

(A) = constant,

(n) depends on the type of electronic transition: (n=1/2) for direct allowed transitions and (n = 2) for indirect allowed transitions [38].

From Fig. 4.7**,** the band gap values were determined by extending the linear part of the curves to the energy axis (X-axis), and the corresponding results are compiled in **Table**

4.2. The incorporation of Ce into the TiO_2 lattice enhances visible light absorption and results in a reduction of the energy band gap. This narrowing of the band gap is likely due to the formation of defect states within the energy gap between the conduction and valence bands of TiO_2 [10]. Furthermore, as the dopant concentration increases, a progressive decrease in band gap energy is observed, leading to improved visible light absorption capacity.

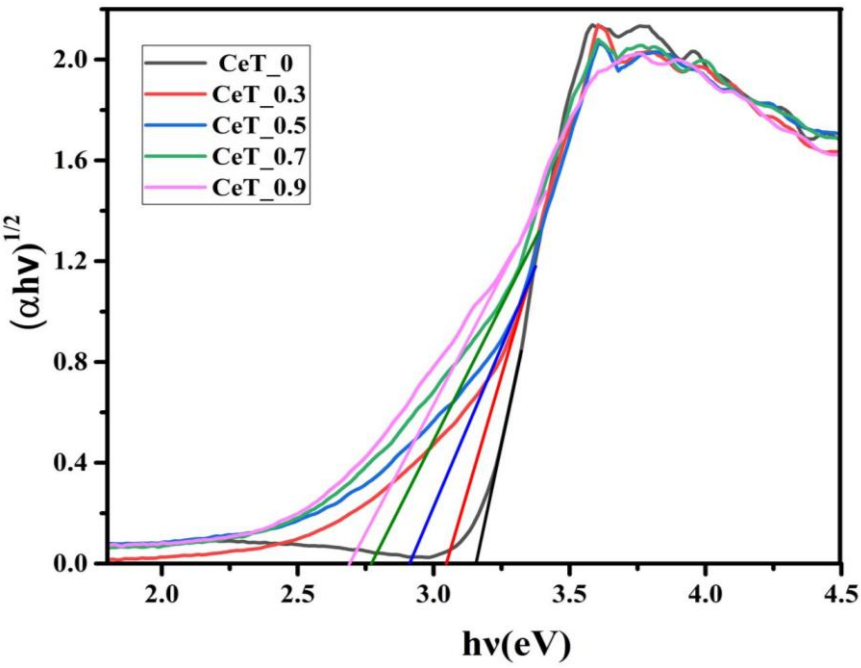

Fig. 4.7 Tauc's plot of prepared samples

Table

4.2 Calculated band gap for prepared samples.

Sample	Calculated bandgap(eV)
CeT_0	3.16
CeT_0.3	3.05
CeT_0.5	2.91
CeT_0.7	2.77
CeT_0.9	2.69

4.7 Photoluminescence Study

Photoluminescence (PL) analysis was carried out to evaluate the electron-hole recombination behavior of the synthesized samples, utilizing an excitation wavelength of 300 nm (F**ig. 4.8)**. The PL spectra revealed prominent emission peaks around 470 nm for all catalysts, which correspond to bound exciton luminescence. Additionally, a secondary peak at approximately 420 nm was observed, attributed to band-edge free exciton luminescence.

As illustrated in F**ig. 4.8,** the PL intensity exhibits an initial decrease followed by an increase with rising dopant concentration. Since photoluminescence results from the recombination of photogenerated electron-hole pairs, the observed variations in intensity reflect changes in their recombination rates. Notably, the **CeT_0.9** sample demonstrated the lowest PL intensity among all tested samples, indicating a suppressed electron-hole recombination rate. This reduced PL intensity suggests that more charge carriers remain available for photocatalytic reactions, thus enhancing the photocatalytic efficiency of the material [13] [22].

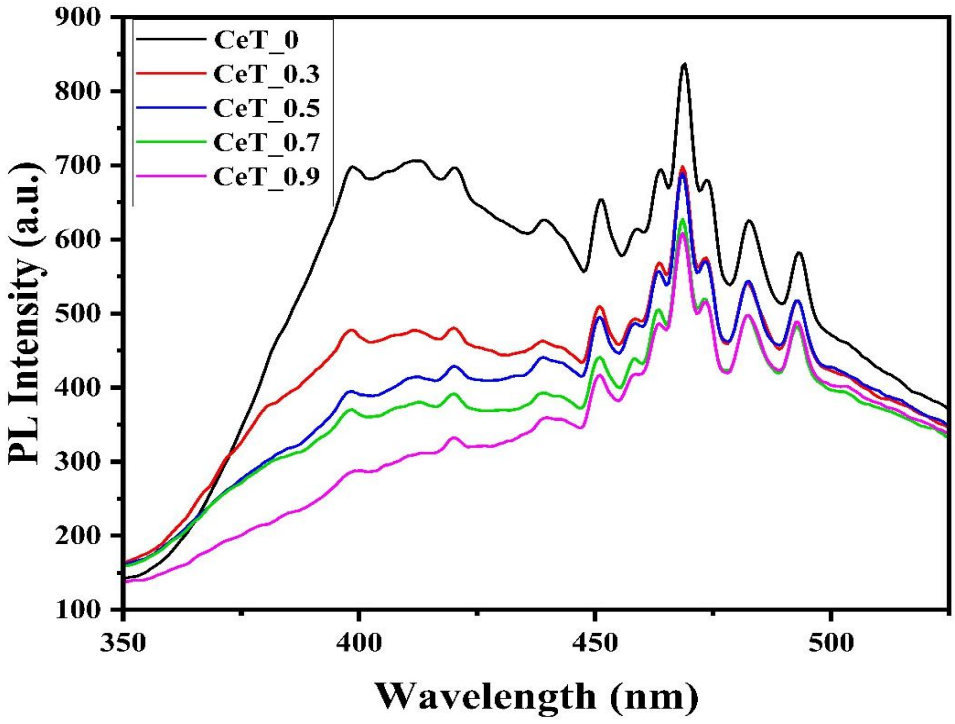

Fig. 4.8 PL spectra of prepared samples

CHAPTER 5

DEGRADATION OF CIPROFLOXACIN ANTIBIOTIC

CHAPTER 5

DEGRADATION OF CIPROFLOXACIN ANTIBIOTIC

5.1 Experiment

The **photocatalytic activity** of the synthesized nanoparticles was evaluated through the degradation of **ciprofloxacin (CIP)** under visible light exposure. The experiments were conducted in a custom-designed reactor equipped with twelve 100-watt bulbs optimized for visible light emission. To ensure stable temperature conditions during the process, two air-circulating fans were incorporated into the reactor system.

For the photocatalytic test, a solution was prepared by dissolving **10 ppm** of CIP in **100 mL** of D.W., followed by the addition of **40 mg** of the photocatalyst. Initially, the suspension was stirred in complete darkness for **30 minutes** to achieve adsorption-desorption equilibrium between the dye molecules and the catalyst surface.

Following this incubation period, the mixture was exposed to visible light in the custom-built reactor to evaluate the photocatalytic degradation activity. During the irradiation phase, small aliquots of the solution were collected at regular intervals of **30 minutes.** These samples were immediately centrifuged to separate the photocatalyst particles from the solution. The clear solution was then analyzed using a **JASCO V-670 UV-Vis spectrophotometer** to monitor the progress of antibiotic degradation.

5.2 Result

Ce-doped TiO_2 nanoparticles were employed to investigate the photocatalytic breakdown of ciprofloxacin (CIP) antibiotic. A 10 ppm CIP solution was prepared using 100 mL of distilled water, and a 40 mg of the catalyst was added into it. The absorption spectra (Fig. 5.1), focusing on the most effective catalyst, CeT_0.9, show a steady decrease in the peak at 269 nm, indicating a decline in antibiotic concentration over time. In dark conditions, a slight reduction in absorption occurs, likely attributed to the adsorption-desorption equilibrium of antibiotic on the catalyst's active sites [38]. When exposed to visible light, the absorption sharply decreases and completely disappears within 120 minutes, confirming the maximum degradation of the CIP.

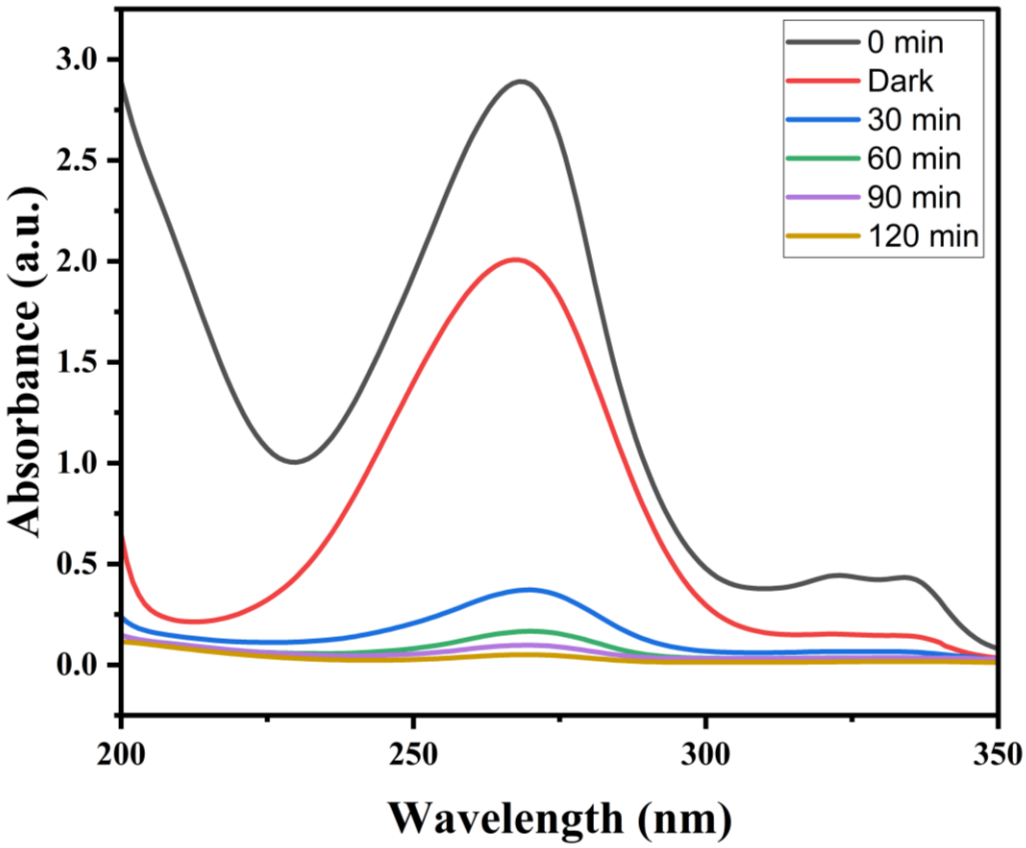

Fig. 5.1 UV-Vis absorption spectra of CIP degradation with CeT_0.9

The Beer-Lambert law was employed to evaluate dye concentration,

$$C = \frac{A}{\varepsilon l} \qquad \text{eq. (5.1)}$$

where A represents absorbance, C indicates the solution's concentration, **ε** is the molar absorption coefficient, and l corresponds to the optical path length.

The sample's degradation efficiency was determined with the following formula:

$$Efficiency(\%) = \left(1 - \left(\frac{C_t}{C_o}\right)\right) \times 100 \qquad \text{eq. (5.2)}$$

Where C_0 represents the initial concentration of the dye and $C_{t\ refers}$ to the concentration at time t [59][15].

Fig. 5.2 demonstrates the plot of the relative antibiotic (CIP) concentration over irradiation time. The results indicate that the CIP concentration decreases significantly upon addition of a photocatalyst under visible light irradiation, demonstrating effective photocatalytic degradation. It is noted from Fig. (5.2) that photocatalyst CeT_0.9 gives

excellent photocatalytic activity than pure TiO_2. Pristine TiO_2 showed the least photocatalytic activity having 82.08% efficiency. The degradation efficiencies for all photocatalysts were computed and condensed in Table 5.1. From Table 5.1, it is observed that the degradation efficiency for CeT_0.9 photocatalyst was found to be 98.25%. The degradation efficiency of CIP increases as doping concentration increases. The increment in efficiency may be due to the increasing number of radicals on the surface, and the decrement in efficiency can be due to the decrement of active sites capturing photogenerated electrons with increasing particle size [60].

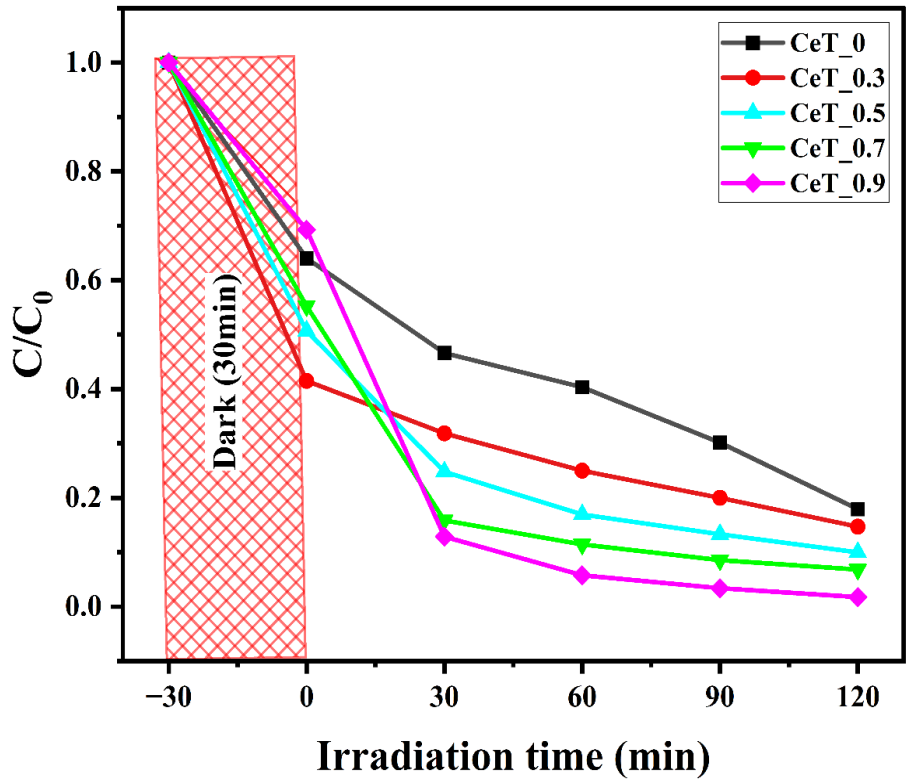

Fig. 5.2 Relative concentration of CIP with irradiation time

The mathematical representation of a first-order kinetic model for photocatalytic reaction is as follows:

$$ln\left(\frac{C_0}{C_t}\right) = kt \qquad \text{eq. (5.3)}$$

where C_0 and C_t denotes initial and time-varying concentrations, k shows the reaction rate and t represents the time of irradiation [61].

The plot of $\ln(C_0/C_t)$ against time is shown in Fig. (5.3). The linear fitting of the plot of $\ln(C_0/C_t)$ against time was used to determine reaction rate k and tabulated in Table (5.1). The reaction rate (k) has a higher value for all the doped samples shows doping of Ce enhances the photocatalytic performance of pure TiO_2.

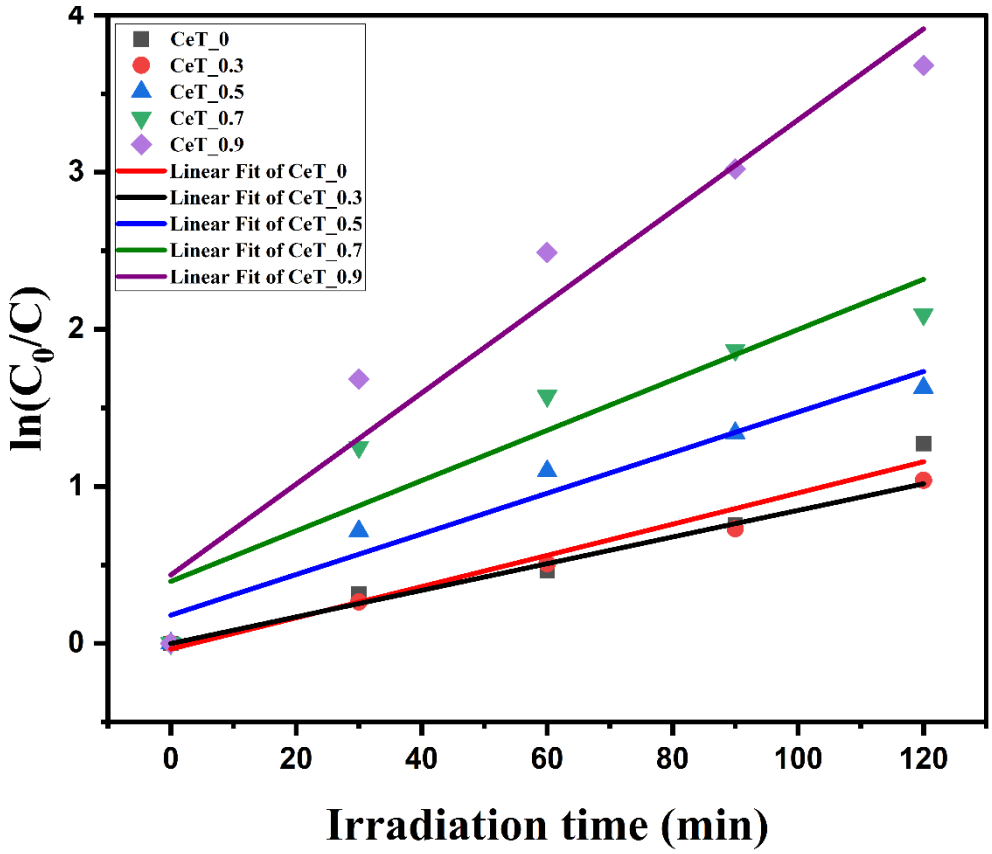

Fig. 5.3 Plot of ln(C0/Ct) against irradiation time

Table 5.1 Determined degradation efficiency and reaction rate of all photocatalyst

Sample Code	Efficiency (%)	Reaction rate (K)
CeT_0.0	82.08	0.00994
CeT_0.3	85.33	0.00848
CeT_0.5	90.05	0.01293
CeT_0.7	93.19	0.01603
CeT_0.9	98.25	0.02899

5.3 Reusability

To assess the stability and reusability of the CeT_0.9 photocatalyst, degradation experiments were performed repeatedly using ciprofloxacin under identical conditions over four consecutive cycles. After each cycle, the photocatalyst was carefully recovered through filtration and thorough washing, ensuring its readiness for subsequent use. As depicted in Fig. 5.5, CeT_0.9 consistently maintained a high photocatalytic efficiency across all four cycles, with only minimal reduction in activity. This sustained performance highlights the excellent structural stability and durability of the catalyst under repeated operational conditions. The ability of CeT_0.9 to retain its degradation efficiency over multiple cycles underscores its robustness and reliability, making it a highly promising candidate for long-term and large-scale wastewater treatment applications. Its notable reusability not only advances environmental sustainability but also significantly enhances the cost-effectiveness and operational feasibility of photocatalytic systems for pharmaceutical pollutant removal and water purification.

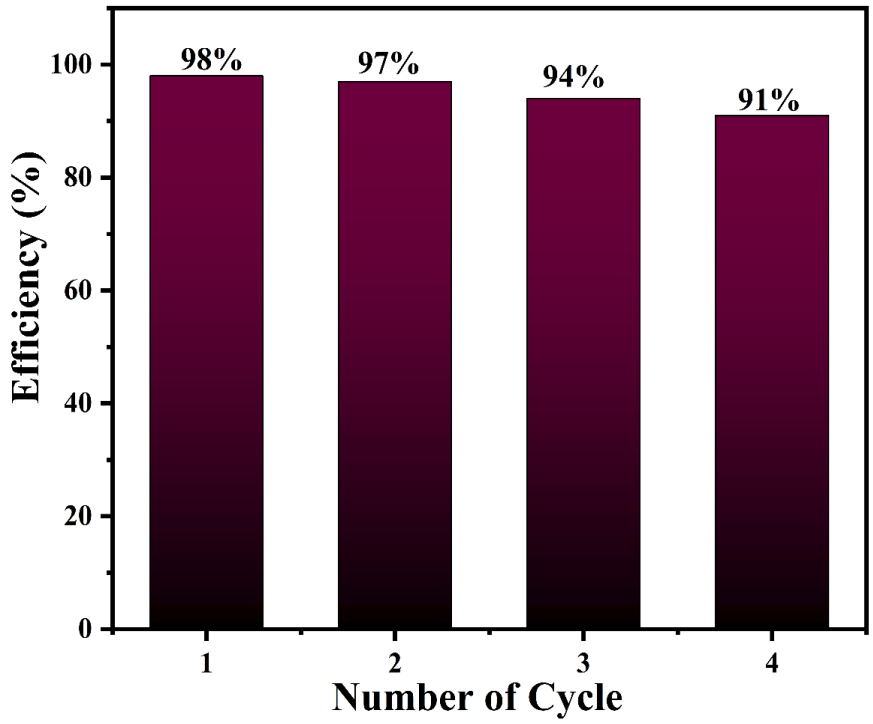

Fig. 5.4 Reusability study for CeT-0.9 Photocatalyst

5.4 Mechanism

The degradation efficiency showed a notable improvement after doping, as evidenced by the results. In Ce-doped TiO_2, the presence of Ce 4f energy levels serve a pivotal role in facilitating interface-mediated charge transfer and effectively suppressing electron-hole recombination. The degradation mechanism of CIP using the CeT_0.9 photocatalyst is depicted in Fig. 5.4. Upon illumination with light, electrons are excited from the valence band to higher energy levels, including the conduction band of TiO_2, generating corresponding holes in the VB.

The step-by-step mechanism [52][19][21] is described below:

1. $TiO_2 + h\nu \rightarrow e^- + h^+$
2. $Ce^{4+} + e^- \rightarrow Ce^{3+}$
3. $Ce^{3+} + O_2 \rightarrow Ce^{4+} + O_2\bullet^-$
4. $O_2\bullet^- + 2H^+ \rightarrow 2\bullet OH$
5. $h^+ + H_2O \rightarrow \bullet OH + H^+$
6. $Dye + \bullet OH \rightarrow CO_2 + H_2O$
7. $Dye + O_2\bullet^- \rightarrow CO_2 + H_2O$

Upon exposure to visible light, the photocatalyst becomes excited, allowing the excited electrons to follow multiple pathways. These electrons can be promoted from the valence band (VB) to the conduction band (CB) of TiO_2, where they are captured by surface-adsorbed oxygen molecules. Alternatively, the electrons may migrate to the Ce 4f energy state, situated just below the Conduction band, reducing Ce^{4+} ions to Ce^{3+}. Subsequently, the Ce^{3+} ions transfer electrons to molecular oxygen, generating superoxide radicals ($O_2^-\bullet$), which play a vital role in facilitating charge carrier separation. These superoxide radicals further react with protons in the solution to produce highly reactive hydroxyl radicals (•OH). Simultaneously, holes remaining in the VB oxidize water molecules, leading to additional hydroxyl radical formation. This cascade of reactions significantly boosts photocatalytic efficiency by enhancing charge separation and producing reactive species that effectively degrade organic contaminants.

The reactive oxygen species (•OH and $O_2^-\bullet$) serve a vital role in degrading organic contaminants like CIP into harmless end products such as water and carbon dioxide. Overall, Ce doping significantly enhances the photocatalytic efficiency of TiO_2 by

reducing electron-hole recombination and promoting more effective charge carrier utilization, leading to improved degradation performance [21] [52].

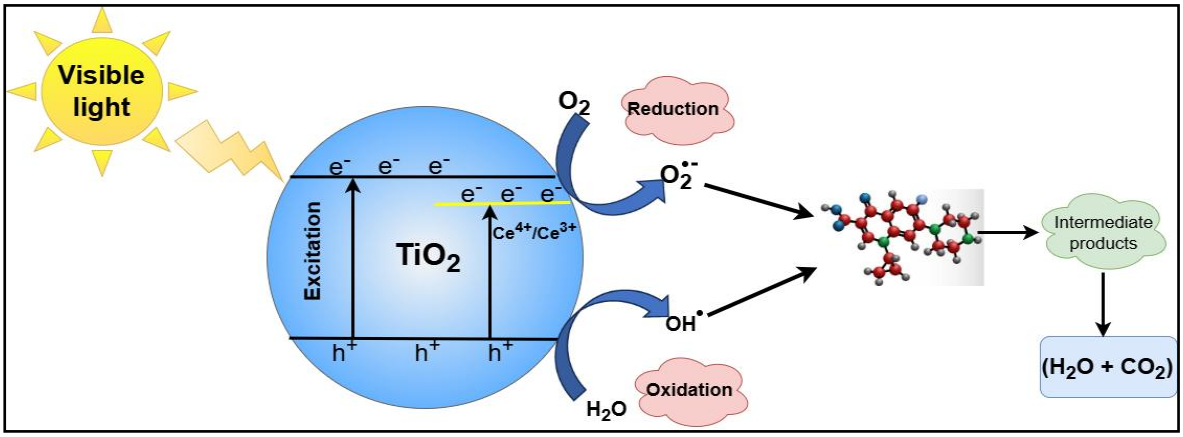

Fig. 5.5 Mechanism of degradation of CIP using prepared sample

CHAPTER 6
CONCLUSION AND FUTURE SCOPE

CHAPTER 6

CONCLUSION AND FUTURE SCOPE

6.1 Conclusion

In this study, Ce-doped TiO_2 nanoparticles were synthesized by hydrothermal method via green synthesis route. XRD analysis demonstrates a reduction in crystallite size with increasing cerium doping levels, while Raman spectroscopy confirmed the presence of anatase phase of TiO_2 in the prepared samples. The presence of functional group and structural modification with Ce doping was analysed by FTIR spectra. SEM images demonstrated that surface morphology was influenced by dopant concentration, and EDS analysis verified the purity of synthesized materials. The decrement in the band gap energy and electron -hole recombination rate with Ce doping was confirmed by UV-Vis and PL studies. The sample with lowest PL intensity CeT_0.9 was carried out for photocatalytic experiments using 10 ppm ciprofloxacin antibiotic with 40 mg of catalyst and the maximum degradation efficiency was found to be **98.25%** within 120 minutes,

6.2 Future Scope

1. Further investigation into the antimicrobial and antibacterial properties of the synthesized Ce-doped TiO_2 nanoparticles.
2. Extending photocatalytic applications to degrade other emerging pollutants such as Bisphenol A, Diclofenac, and Tetracycline.
3. Exploring the potential of these materials for self-cleaning surfaces and coatings.
4. Assessing their efficacy in air purification systems for removing airborne contaminants.

References

[1] M. Dhiman, L. Sharma, P. Kaushik, A. Singh, and M. M. Sharma, “Correction: Dhiman et al. Mycorrhiza: An Ecofriendly Bio-Tool for Better Survival of Plants in Nature. Sustainability 2022, 14, 10220,” 2024. doi: 10.3390/su16177723.

[2] R. A. Rayan, “Pharmaceutical effluent evokes superbugs in the environment: A call to action,” *Biosaf. Heal.*, vol. 5, no. 6, pp. 363–371, 2023, doi: https://doi.org/10.1016/j.bsheal.2023.10.005.

[3] T. Zhang *et al.*, “Enhanced photocatalytic activity of TiO2 with acetylene black and persulfate for degradation of tetracycline hydrochloride under visible light,” *Chem. Eng. J.*, vol. 384, p. 123350, 2020, doi: https://doi.org/10.1016/j.cej.2019.123350.

[4] S. Dutta *et al.*, “Contamination of textile dyes in aquatic environment: Adverse impacts on aquatic ecosystem and human health, and its management using bioremediation,” *J. Environ. Manage.*, vol. 353, p. 120103, 2024, doi: https://doi.org/10.1016/j.jenvman.2024.120103.

[5] S. J. Olusegun, G. Larrea, M. Osial, K. Jackowska, and P. Krysinski, “Photocatalytic Degradation of Antibiotics by Superparamagnetic Iron Oxide Nanoparticles. Tetracycline Case,” 2021. doi: 10.3390/catal11101243.

[6] N. Kamal, A. K. Saha, E. Singh, A. Pandey, and P. C. Bhargava, “Biodegradation of ciprofloxacin using machine learning tools: Kinetics and modelling,” *J. Hazard. Mater.*, vol. 470, p. 134076, 2024, doi: https://doi.org/10.1016/j.jhazmat.2024.134076.

[7] “Ciprofloxacin | C17H18FN3O3 | CID 2764 - PubChem.” Accessed: May 11, 2025. [Online]. Available: https://pubchem.ncbi.nlm.nih.gov/compound/Ciprofloxacin

[8] B. Khanizadeh, M. Khosravi, M. A. Behnajady, A. Shamel, and B. Vahid, “Mg and La Co-doped ZnO nanoparticles prepared by sol– gel method: Synthesis, characterization and photocatalytic activity,” *Period. Polytech. Chem. Eng.*, vol. 64, no. 1, pp. 61–74, 2020, doi: 10.3311/PPch.12959.

[9] K. T. Karthikeyan, A. Nithya, and K. Jothivenkatachalam, “Photocatalytic and antimicrobial activities of chitosan-TiO2 nanocomposite,” *Int. J. Biol. Macromol.*, vol. 104, pp. 1762–1773, 2017, doi:

https://doi.org/10.1016/j.ijbiomac.2017.03.121.

[10] S. M. Fernandes *et al.*, “Maximizing photocatalytic efficiency with minimal amount of gold: Solar-driven TiO2 photocatalysis supported by MICROSCAFS® for facile catalyst recovery,” *J. Environ. Chem. Eng.*, vol. 12, no. 2, p. 112043, 2024, doi: https://doi.org/10.1016/j.jece.2024.112043.

[11] F. Hayat *et al.*, “Biological activity of silver nanoparticles synthesized from untapped secondary metabolites of Olea europea endophytic Bacillus amyloliquefaciens,” *PLoS One*, vol. 20, May 2025, doi: 10.1371/journal.pone.0321134.

[12] F. Zhang *et al.*, “Recent Advances and Applications of Semiconductor Photocatalytic Technology,” 2019. doi: 10.3390/app9122489.

[13] C. Huang *et al.*, “Eu-doped TiO2 nanoparticles with enhanced activity for CO2 phpotcatalytic reduction,” *J. CO2 Util.*, vol. 26, pp. 487–495, 2018, doi: https://doi.org/10.1016/j.jcou.2018.06.004.

[14] N. Joudeh and D. Linke, “Nanoparticle classification, physicochemical properties, characterization, and applications: a comprehensive review for biologists,” *J. Nanobiotechnology*, vol. 20, no. 1, p. 262, 2022, doi: 10.1186/s12951-022-01477-8.

[15] G. K. Sukhadeve, S. Y. Janbandhu, R. Kumar, D. H. Lataye, D. D. Ramteke, and R. S. Gedam, “Visible light assisted photocatalytic degradation of Indigo Carmine dye and NO2 removal by Fe doped TiO2 nanoparticles,” *Ceram. Int.*, vol. 48, no. 19, Part B, pp. 29121–29135, 2022, doi: https://doi.org/10.1016/j.ceramint.2022.05.053.

[16] R. Savitha, R. Raghunathan, and R. Chetty, “Enhanced visible light sensitized photoreaction by mixed phase titania nanotubes,” *Appl. Surf. Sci.*, vol. 609, p. 155252, 2023, doi: https://doi.org/10.1016/j.apsusc.2022.155252.

[17] V. Etacheri, C. Di Valentin, J. Schneider, D. Bahnemann, and S. C. Pillai, “Visible-light activation of TiO2 photocatalysts: Advances in theory and experiments,” *J. Photochem. Photobiol. C Photochem. Rev.*, vol. 25, pp. 1–29, 2015, doi: https://doi.org/10.1016/j.jphotochemrev.2015.08.003.

[18] K. Wang, N. Yang, and B. Xiao, “Vacancies for the Visible-Light Photocatalytic Hydrogen Production,” pp. 1–20.

[19] V. Štengl, S. Bakardjieva, and N. Murafa, “Preparation and photocatalytic activity

of rare earth doped TiO2 nanoparticles," *Mater. Chem. Phys.*, vol. 114, no. 1, pp. 217–226, 2009, doi: https://doi.org/10.1016/j.matchemphys.2008.09.025.

[20] M. Bellardita, A. Di Paola, L. Palmisano, F. Parrino, G. Buscarino, and R. Amadelli, "Preparation and photoactivity of samarium loaded anatase, brookite and rutile catalysts," *Appl. Catal. B Environ.*, vol. 104, no. 3, pp. 291–299, 2011, doi: https://doi.org/10.1016/j.apcatb.2011.03.016.

[21] A. S. Gadge, S. Y. Janbandhu, and R. S. Gedam, "Exploring the photocatalytic and antibacterial activity of Ce-doped TiO2 nanoparticles with remarkable self-cleaning superhydrophilic surface for outdoor application," *Ceram. Int.*, vol. 51, no. 1, pp. 602–611, 2025, doi: https://doi.org/10.1016/j.ceramint.2024.11.038.

[22] K. A. Ali, A. Z. Abdullah, and A. R. Mohamed, "Visible light responsive TiO2 nanoparticles modified using Ce and La for photocatalytic reduction of CO2: Effect of Ce dopant content," *Appl. Catal. A Gen.*, vol. 537, pp. 111–120, 2017, doi: https://doi.org/10.1016/j.apcata.2017.03.022.

[23] S. P. Patil and P. M. Rane, "Psidium guajava leaves assisted green synthesis of metallic nanoparticles: a review," *Beni-Suef Univ. J. Basic Appl. Sci.*, vol. 9, no. 1, p. 60, 2020, doi: 10.1186/s43088-020-00088-2.

[24] P. Biswas *et al.*, "Betelvine (Piper betle L.): A comprehensive insight into its ethnopharmacology, phytochemistry, and pharmacological, biomedical and therapeutic attributes," *J. Cell. Mol. Med.*, vol. 26, no. 11, pp. 3083–3119, 2022, doi: 10.1111/jcmm.17323.

[25] J. Gaur *et al.*, "Eco-friendly innovation: harnessing nature's blueprint for enhanced photocatalysis and antimicrobial potential in multi-structured PN/ZnO nanoparticles," *Funct. Compos. Struct.*, vol. 6, no. 1, 2024, doi: 10.1088/2631-6331/ad2c10.

[26] J.-K. Oh, J.-K. Lee, S. J. Kim, and K.-W. Park, "Synthesis of phase- and shape-controlled TiO2 nanoparticles via hydrothermal process," *J. Ind. Eng. Chem.*, vol. 15, no. 2, pp. 270–274, 2009, doi: https://doi.org/10.1016/j.jiec.2008.10.001.

[27] S. M. Hunagund *et al.*, "Photocatalysis effect of a novel green synthesis gadolinium doped titanium dioxide nanoparticles on their biological activities," *J. Photochem. Photobiol. A Chem.*, vol. 346, pp. 159–167, 2017, doi: https://doi.org/10.1016/j.jphotochem.2017.06.003.

[28] G. K. Sukhadeve, H. Bandewar, S. Y. Janbandhu, J. R. Jayaramaiah, and R. S.

Gedam, “Photocatalytic hydrogen production, dye degradation, and antimicrobial activity by Ag-Fe co-doped TiO2 nanoparticles,” *J. Mol. Liq.*, vol. 369, p. 120948, 2023, doi: https://doi.org/10.1016/j.molliq.2022.120948.

[29] E. Cerrato, E. Gaggero, P. Calza, and M. C. Paganini, “The role of Cerium, Europium and Erbium doped TiO2 photocatalysts in water treatment: A mini-review,” *Chem. Eng. J. Adv.*, vol. 10, p. 100268, 2022, doi: https://doi.org/10.1016/j.ceja.2022.100268.

[30] S. Bhullar, N. Goyal, and S. Gupta, “Rapid green-synthesis of TiO2nanoparticles for therapeutic applications,” *RSC Adv.*, vol. 11, no. 48, pp. 30343–30352, 2021, doi: 10.1039/d1ra05588g.

[31] P. M. Thanikachallam, M. Keerthana, R. Sangavi, A. Nagaraj, and K. P, “Comparative analysis of green synthesis of TiO2 nanoparticles using four different leaf extract,” *Mater. Today Proc.*, vol. 40, Sep. 2020, doi: 10.1016/j.matpr.2020.08.438.

[32] H. Khan, “Sol-Gel Synthesis of TiO2 from TiOSO4 (Part 2): Kinetics and Photocatalytic Efficiency of Methylene Blue Degradation Under UV Irradiation,” 2025. doi: 10.3390/catal15010064.

[33] A. Saka *et al.*, “Biosynthesis of TiO2 nanoparticles by Caricaceae (Papaya) shell extracts for antifungal application,” *Sci. Rep.*, vol. 12, no. 1, p. 15960, 2022, doi: 10.1038/s41598-022-19440-w.

[34] A. S. Gadge, P. Bobde, V. Ganesh, and R. S. Gedam, “Novel green synthesis of Gd-doped TiO2 nanoparticles for environmental remediation: statistical modeling and process optimization,” *New J. Chem.*, vol. 49, no. 14, pp. 5995–6011, 2025, doi: 10.1039/D5NJ00856E.

[35] A. Diego-Rucabado *et al.*, “Visible Light Active Ce-Doped and Cu–Ce co-doped TiO2 Nanocrystals and Optofluidics for Clean Alcohol Production from CO2,” *ACS Sustain. Chem. Eng.*, vol. 11, no. 36, pp. 13260–13273, Sep. 2023, doi: 10.1021/acssuschemeng.3c01925.

[36] M. Nasir, S. Bagwasi, Y. Jiao, F. Chen, B. Tian, and J. Zhang, “Characterization and activity of the Ce and N co-doped TiO2 prepared through hydrothermal method,” *Chem. Eng. J.*, vol. 236, pp. 388–397, 2014, doi: https://doi.org/10.1016/j.cej.2013.09.095.

[37] H. Liu, M. Wang, Y. Wang, Y. Liang, W. Cao, and Y. Su, “Ionic liquid-templated

synthesis of mesoporous CeO2–TiO2 nanoparticles and their enhanced photocatalytic activities under UV or visible light," *J. Photochem. Photobiol. A Chem.*, vol. 223, no. 2, pp. 157–164, 2011, doi: https://doi.org/10.1016/j.jphotochem.2011.06.014.

[38] A. S. Gadge, S. Y. Janbandhu, G. K. Sukhadeve, R. Kumar, C. D. Gajbhiye, and R. S. Gedam, " TiO 2 Nanoparticles for Methylene Blue Dye Degradation: Effect of Calcination Temperature ," *ECS J. Solid State Sci. Technol.*, vol. 12, no. 8, p. 086004, 2023, doi: 10.1149/2162-8777/acf06f.

[39] A. A. Bunaciu, E. gabriela Udriştioiu, and H. Y. Aboul-Enein, "X-Ray Diffraction: Instrumentation and Applications," *Crit. Rev. Anal. Chem.*, vol. 45, no. 4, pp. 289–299, 2015, doi: 10.1080/10408347.2014.949616.

[40] P. Rostron, S. Gaber, and D. Gaber, "Raman Spectroscopy , Review," no. September, 2016.

[41] K. D. Vernon-Parry, "Scanning electron microscopy: an introduction," *III-Vs Rev.*, vol. 13, no. 4, pp. 40–44, 2000, doi: https://doi.org/10.1016/S0961-1290(00)80006-X.

[42] A. Kumar and K. S. Prasad, "Role of nano-selenium in health and environment," *J. Biotechnol.*, vol. 325, pp. 152–163, 2021, doi: https://doi.org/10.1016/j.jbiotec.2020.11.004.

[43] A. Gacem *et al.*, "Plasmon Inspired 2D Carbon Nitrides: Structural, Optical and Surface Characteristics for Improved Biomedical Applications," *Crystals*, vol. 12, Aug. 2022, doi: 10.3390/cryst12091213.

[44] G. D. Gilliland, "Photoluminescence spectroscopy of crystalline semiconductors," *Mater. Sci. Eng. R Reports*, vol. 18, no. 3, pp. 99–399, 1997, doi: https://doi.org/10.1016/S0927-796X(97)80003-4.

[45] D. Patel, D. Panchal, K. Patel, M. Dalwadi, and U. Upadhyay, '"A Review on UV Visible Spectroscopy,'" *Int. J. Creat. Res. T*, vol. 10, no. 5, pp. 1–13, 2022, doi: 10.35629/7781-070511441151.

[46] L. A.K, I. V Viswanath, D. Bhagavathula, G. Boddeti, R. Venu, and Y. L. N. Murthy, "Review on nanomaterials: Synthesis and applications," *Mater. Today Proc.*, vol. 18, Aug. 2019, doi: 10.1016/j.matpr.2019.07.371.

[47] C. Berthomieu and R. Hienerwadel, "Fourier transform infrared (FTIR) spectroscopy," *Photosynth. Res.*, vol. 101, pp. 157–170, Jul. 2009, doi:

10.1007/s11120-009-9439-x.

[48] M. Viana, V. F. Soares, and N. Mohallem, “Synthesis and characterization of TiO2 nanoparticles,” *Ceram. Int.*, vol. 36, pp. 2047–2053, Sep. 2010, doi: 10.1016/j.ceramint.2010.04.006.

[49] V. Stengl, S. Bakardjieva, and N. Murafa, “Preparation and Photocatalytic Activity of Rare Earth Doped TiO2 Nanoparticles,” *Mater. Chem. Phys.*, vol. 114, pp. 217–226, Mar. 2009, doi: 10.1016/j.matchemphys.2008.09.025,.

[50] J. Xie *et al.*, “Preparation and characterization of monodisperse Ce-doped TiO2 microspheres with visible light photocatalytic activity,” *Colloids Surfaces A Physicochem. Eng. Asp.*, vol. 372, no. 1, pp. 107–114, 2010, doi: https://doi.org/10.1016/j.colsurfa.2010.09.037.

[51] Z. Fan, F. Meng, J. Gong, H. Li, Z. Ding, and B. Ding, “One-step hydrothermal synthesis of mesoporous Ce-doped anatase TiO2 nanoparticles with enhanced photocatalytic activity,” *J. Mater. Sci. Mater. Electron.*, vol. 27, Nov. 2016, doi: 10.1007/s10854-016-5329-0.

[52] L. Mansouri, V. Srivastava, M. Sillanpää, and L. Bousselmi, “Enhancement of Eu and Ce doped TiO2 Thin Films Photoactivity: Application on Amido Black Photodegradation,” *Inorg. Chem. Commun.*, vol. 133, p. 108912, Sep. 2021, doi: 10.1016/j.inoche.2021.108912.

[53] V. Ndabankulu, S. Maddila, and S. Jonnalagadda, “Synthesis of lanthanide-doped TiO2 nanoparticles and their photocatalytic activity under visible light,” *Can. J. Chem.*, vol. 97, pp. 672–681, Jun. 2019, doi: 10.1139/cjc-2018-0408.

[54] Z. N. Kayani, Maria, S. Riaz, and S. Naseem, “Magnetic and antibacterial studies of sol-gel dip coated Ce doped TiO2 thin films: Influence of Ce contents,” *Ceram. Int.*, vol. 46, no. 1, pp. 381–390, 2020, doi: https://doi.org/10.1016/j.ceramint.2019.08.272.

[55] S. Shanavas, A. Priyadharsan, V. Vasanthakumar, A. Arunkumar, P. M. Anbarasan, and S. Bharathkumar, “Mechanistic investigation of visible light driven novel La2CuO4/CeO2/rGO ternary hybrid nanocomposites for enhanced photocatalytic performance and antibacterial activity,” *J. Photochem. Photobiol. A Chem.*, vol. 340, pp. 96–108, 2017, doi: https://doi.org/10.1016/j.jphotochem.2017.03.002.

[56] V. Ndabankulu, S. Maddila, and S. Jonnalagadda, “Ceria doped TiO 2 as

photocatalyst for water treatment under visible light," *IOP Conf. Ser. Mater. Sci. Eng.*, vol. 668, p. 12011, Nov. 2019, doi: 10.1088/1757-899X/668/1/012011.

[57] X. Jaramillo-Fierro and R. León, "Effect of Doping TiO2 NPs with Lanthanides (La, Ce and Eu) on the Adsorption and Photodegradation of Cyanide—A Comparative Study," *Nanomaterials*, vol. 13, p. 1068, Mar. 2023, doi: 10.3390/nano13061068.

[58] A.-W. Xu, Y. Gao, and H.-Q. Liu, "The Preparation, Characterization, and their Photocatalytic Activities of Rare-Earth-Doped TiO2 Nanoparticles," *J. Catal.*, vol. 207, no. 2, pp. 151–157, 2002, doi: https://doi.org/10.1006/jcat.2002.3539.

[59] S. Janbandhu, S. Munishwar, G. Sukhadeve, and R. Gedam, "Effect of annealing time on optical properties of CdS QDs containing glasses and their application for degradation of methyl orange dye," *Mater. Charact.*, vol. 152, Apr. 2019, doi: 10.1016/j.matchar.2019.04.027.

[60] G. Khade, N. Gavade, M. Suwarnkar, D. M. Dhanavade, and K. Sonawane, "Enhanced photocatalytic activity of europium doped TiO2 under sunlight for the degradation of methyl orange," *J. Mater. Sci. Mater. Electron.*, vol. 1, p. 1, Aug. 2017, doi: 10.1007/s10854-017-6883-9.

[61] Z. Tianhu *et al.*, "Enhanced photocatalytic activity of TiO2 with acetylene black and persulfate for degradation of tetracycline hydrochloride under visible light," *Chem. Eng. J.*, vol. 384, p. 123350, Nov. 2019, doi: 10.1016/j.cej.2019.123350.